Remote field eddy current probes for the detection of stress corrosion cracks in transmission pipelines

by

Plamen Alexandrov Ivanov

A dissertation submitted to the graduate faculty

in partial fulfillment of the requirements for the degree of

DOCTOR OF PHILOSOPHY

Major: Electrical Engineering (Communications and Signal Processing)

Program of Study Committee:
Lalita Udpa, Major Professor
David Jiles
Frank Peters
Yushi Sun
Satish Udpa
Robert Weber

Iowa State University

Ames, Iowa

2002

Graduate College
Iowa State University

This is to certify that the doctoral dissertation of

Plamen Alexandrov Ivanov

has met the dissertation requirements of Iowa State University

Lalita Udpa
Major Professor

Vinay Vittal
For the Major Program

TABLE OF CONTENTS

LIST OF FIGURES

IS-T 2354

ABSTRACT

Magnetic flux leakage (MFL) is a technique used widely in non-destructive testing (NDT) of natural gas and petroleum transmission pipelines. This inspection method relies on magnetizing the pipe-wall in axial direction. The MFL inspection tool is equipped with an array of Hall sensors located around the circumference of the pipe, which registers the flux leakage caused by any defects present in the pipe-wall. Currently, the tool magnetizes the pipewall in axial direction making it largely insensitive to axially oriented defects. One type of defect, which is of a growing concern in the gas and petroleum industry is the stress corrosion crack (SCC). The SCCs are a result of aging, corrosion, fatigue and thermal stresses. SCCs are predominantly axially oriented and are extremely tight, which makes them impossible to be detected using current inspection technology.

A possible solution to this problem is to utilize the remote field eddy current (RFEC) effect to detect axially oriented defects. The RFEC method has been widely used in industry in the inspection of tubular products. The method uses a pair of excitation and pick-up coils. The pick-up coil located in the remote field region, usually two, three pipe-diameters away from the excitation coil. With RFEC the presence of defects is detected by the disturbance in the phase of the signal measured by the pick-up coil relative to that of the excitation coil. Unlike conventional eddy current testing the RFEC method is sensitive to defects on the exterior of the inspected product, which makes it a good candidate for the development of in-line inspection technology.

This work focuses on the development of non-destructive testing technique, which uses remote field eddy currents induced by rotating magnetic field (RMF). A major advantage of the RMF is that it makes possible to not only detect a defect but also localize its position in circumferential direction. Also, it could potentially allow detection of defects, regardless of their shape and orientation. In this work the RFEC-RMF technique is investigated and is shown to be useful tool in the detection of axially oriented, circumferentially oriented and skewed notches, SCCs and round defects. Finally, a data acquisition system is designed, capable of performing the RFEC-RMF measurements automatically.

CHAPTER 1. INTRODUCTION

Natural gas is transmitted to customers in the United States, through a supply network totaling over 1 million miles of pipelines. The network contains critical structures exposed to the harsh natural environment. The maintenance of these structures requires the highest level of confidence in non-destructive evaluation (NDE) techniques, used for inspection. Mechanical damage has been recognized as the leading cause of pipeline failure, followed by material defects, corrosion and others. Stress corrosion cracking (SCC) was first identified as a cause of failure, which occurred in 1965 in Nachitoches, Louisiana. So far 1.5% of pipeline failures have been attributed to SCC. Although SCC is known as a failure mechanism in other industries, it is a relatively new cause of concern for the gas transmission industry [1] and technology for detection of SCC is yet to be developed [2].

SCC results from the combined action of stress, electrochemical environment and temperature [3]. Once initiated cracks tend to grow in a susceptible steel pipeline. When a combination of suitable conditions exists on a pipe surface, the cathodic current on a line can help to initiate the formation of an SCC. Until 1965 it was thought that the natural soil environments would not be capable of producing SCC in the relatively resistant pipeline steel. Since then more than 80 service leaks or ruptures have been attributed to SCC. Soon after the Nachitoches failure it became apparent, that although the frequency of failures attributed to SCC is quite low, compared to other causes, they occur from time to time and research investigating the cause was warranted. Since then much has been learned about the nature of SCC. Studies have been initiated to evaluate the feasibility of preventative measures. It became obvious that the problem of SCC in buried pipes is quite complex and requires a lot of work before adequate inspection technology and preventative measures can be developed.

1.1. Characteristics of stress corrosion cracking

Stress corrosion cracks have several unique features, not found in any other types of defect causing failure conditions [4]. The cracks are branched, they are usually found to occur in colonies, and they usually contain corrosion deposit. They can be inter-granular or trans-granular depending on the material type and environment. The environments leading to corrosion cracking are usually mildly corrosive; therefore severe corrosion is not associated or found in combination with SCC. Although some pitting corrosion has been found around SCC, no general or pitting corrosion has been found in the SCC related failures that have been studied. SCCs are generally oriented perpendicular to the maximum stress. In a pressurized pipeline the maximum stress is usually in circumferential direction and therefore SCC occur primarily in axial direction.

SCCs usually occur in colonies. Colonies are considered "sparse" if cracks are far apart in circumferential direction (shown on Figure 1.1) and "dense" otherwise (shown in Figure 1.2). The circumferential distance between the adjacent cracks in a colony can be up to several times the pipe wall thickness. The axial distance between the cracks in colonies in pipes that experienced failure can be from overlapping to several times the wall thickness. Cracks can be shallow or very deep. Many of the cracks found in dense colonies tend to be shallow. Cracks in sparse colonies can grow until they reach nearly through the wall, which causes a pipeline to rupture. Moreover, cracks can grow in length and "join" other cracks in the colony.

SCC can be inter-granular, in which the cracking path occurs along the grain boundaries in the material or trans-granular in which the cracking path crossing through the grain structure of the material. Trans-granular fracture surfaces are smoother than inter-granular. Two other types of SCC are high pH and low pH cracks. High pH cracks are typically inter-granular, but can become trans-granular when their depth increases. High pH cracks are usually filled with oxide and show little separation between the crack faces or in other words they are very tight [5], which would present a considerable challenge in NDT inspection. Low pH cracking is often trans-granular. The crack sides are usually well separated and contain loosely adherent corrosion products in the crack volume [6]. The shape

of the stress corrosion colony depends on the type of environment and coating conditions. Deep cracks are of primary concern in inspection and evaluation of pipeline integrity.

Figure1.1. Sparse stress corrosion cracking colony [3]

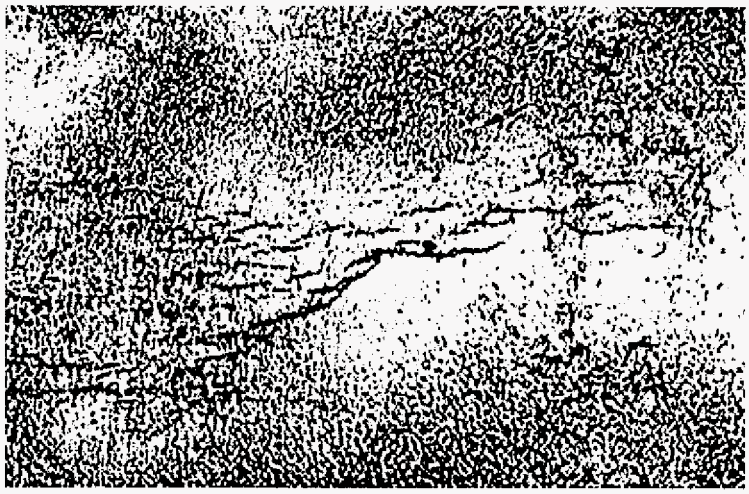

Figure 1.2. Dense stress corrosion cracking colony [3]

1.2. Current pipeline inspection technology

The most commonly used method of in-line inspection today is based on magnetic flux leakage (MFL) phenomenon. The MFL method of inspection is illustrated in figure 1.3. When a pipe wall is magnetized in the presence of a defect the magnetic field is redistributed. The field in the area around the defect 'leaks' and is directed out of the material and can be registered using a sensor located close to the wall surface. The method utilizes a high level of magnetization, which is usually achieved using either electromagnets or extremely strong permanent magnets, based on materials doped with rear earth elements.

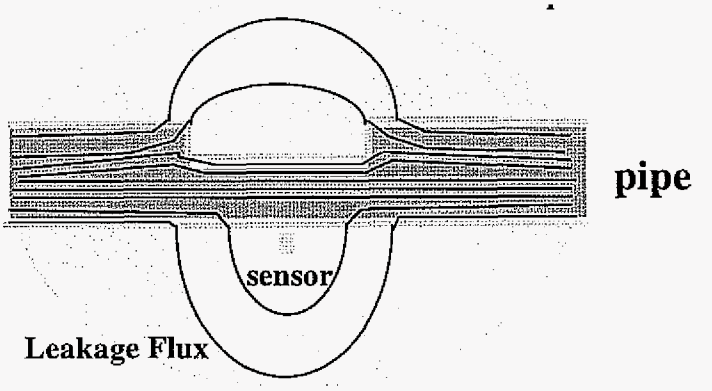

Figure 1.3. Magnetic flux leakage method of inspection

Electro-magnetic inspection tools based on the MFL principle are commonly used in-line inspection technology. The tool is inserted in a pipeline and is propelled by the pressure of the gas transported in it. An array of sensors mounted circumferentially monitors the changes in the leakage field near the internal surface of the pipeline as well as all possible changes in the internal geometry of the pipe. Figure 1.4 shows a schematic of an MFL inspection tool, commonly referred to as "pig".

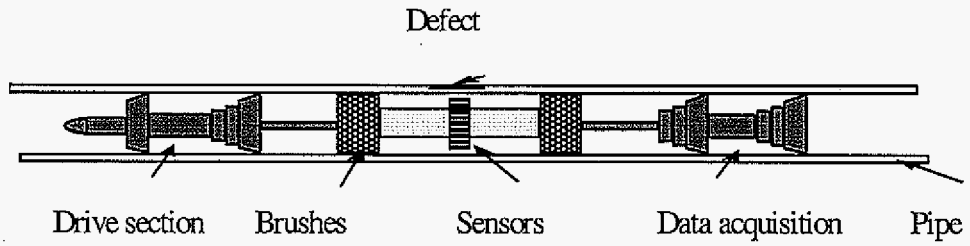

Figure 1.4. MFL inspection tool

The tool consists of the following major parts: magnetic circuit, hall sensor array, data acquisition electronics and supporting polyurethane cups. The magnetic circuit consists of magnet assembly, backing iron and brushes. The poles of the magnet are in contact with the pipe wall via flexible metal brushes, which compensate for changes in the pipeline internal diameter. The electronics is contained in a rugged vessel capable of withstanding the pressures of the fluid in the pipeline. The sensors are used to detect the leakage field.

The MFL tool magnetizes the pipe to near saturation level and records the flux leakage due to anomalies that occur inside the pipe where there are external or internal defects (mostly metal loss or mechanical damage) [7]. The shapes of leakage fields around defects in ferromagnetic materials have been a subject of intensive research. The results have been well documented and reported in the literature [8], [9]. It has been shown that for general metal loss, caused by corrosion and for mechanical damage defects the MFL method of inspection has emerged as a reliable NDT technique of choice, capable of high performance under the extreme operating conditions in the field.

However, the MFL tool is not capable of detecting axially oriented SCC, because in this case the crack walls do not intersect the axially oriented magnetic field. The tool primarily magnetizes the pipe wall in axial direction. The SCCs are oriented mostly axially and therefore would not generate leakage field that can be detected. It is possible that circumferentially oriented cracks would cause enough field disturbances to be detected, but not axially oriented tight SCCs. Therefore the MFL technique is not suitable for detection of cracks that are aligned axially [10].

An alternate method for axial SCC detection in pipes in based on the current perturbation method described below. The speed with which the MFL tool moves through the

pipeline affects the field distribution by introducing significant motion-induced currents in the conducting pipe wall. Experiments [11] suggest that, for typical pipeline MFL tools, the time constant for the magnetic flux to diffuse through the pipe wall can be comparable to the transit time. Since pipeline steel is a conducting ferromagnetic material the changing magnetic flux occurring in the pipe wall during the passage of an MFL inspection tool generate induced currents that are circumferentially oriented. These induced currents obstruct the diffusion of magnetic flux through the pipe wall. Consequently, significant changes in the anomalous MFL patterns induced by defects, particularly for outer diameter can be expected. The question of whether velocity effects are significant depends on the relation of magnetic diffusion time constant to detector transit time. Efforts to test moving assemblies with a damaged pipe mounted above the test assembly in laboratory conditions found that motion dramatically affects performance [11].

Measurements show that in-line inspection tool speed can cause significant reduction in defect-induced axial and radial MFL signals. On the other hand the motion-induced currents are oriented circumferentially and they are orthogonal to axially oriented SCC as illustrated in figure 1.5. Detection of the interaction between the circumferentially oriented currents and axially oriented cracks constitutes the principle of the current perturbation method [12], [13]. Current perturbation has also been studied as a candidate technique for SCC detection.

Alternately, SCCs can be detected by using a magnet assembly, which would produce circumferentially oriented magnetic field. This field would intersect an axially oriented crack. Such an assembly is illustrated in figure 1.6. In this case the magnet is oriented radially. However this solution would require multiple magnet and sensor assemblies to cover blind areas indicated by points A and B.

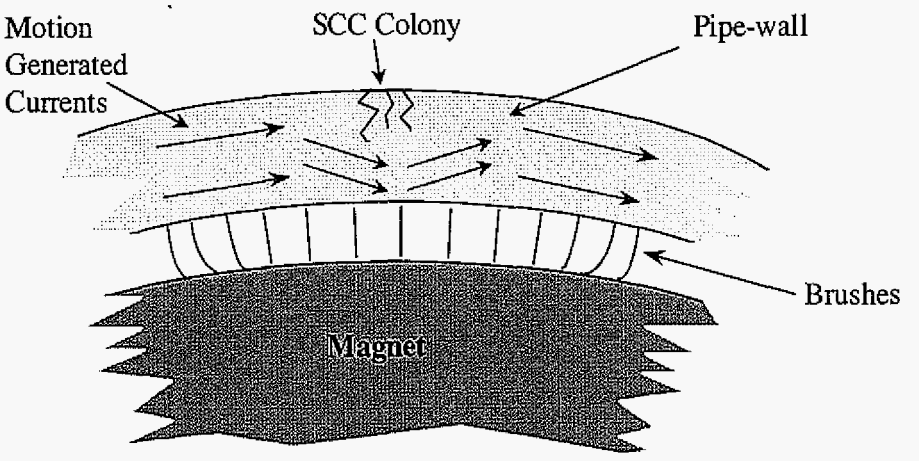

Figure 1.5. Motion induced currents in circumferential direction

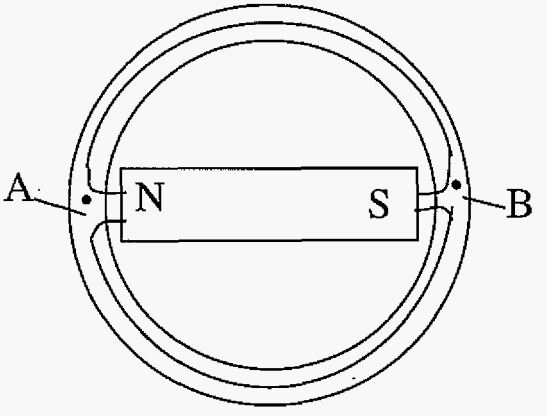

Figure 1.6. Magnetic field distribution from radially oriented magnet

This thesis proposes a new approach for detecting axially oriented cracks by using a circumferential magnetic flux orientation in space where the direction of flux rotates with time. The rotating magnetic field (RMF) method is an implementation of this approach. The advantages of rotating magnetic field have been reported in literature [14], [15]. Enokizono, Nagata and Oka in [16], [17] use this principle to detect defects on the opposite side of a conductive plate. They have developed an integrated sensor assembly, which consists of a

ferrite core with two exiting coils wound with axes perpendicular to each other. The coils are driven with 10 Hz currents that are 90 degrees apart, so that the two phases generate a rotating magnetic field. Another row of pick-up coils serves as flux density sensors. The authors report that they were able to detect and accurately locate the defect on the opposite side of a plate.

A classical solution, where three phases 120 degrees apart generate the rotating magnetic field is well known and has been used in AC electric power generators and motors. Every aspect of the design, performance, magnetic flux density distribution of these devices has been studied and described in the literature, but only recently the RMF method has been studied as a potential candidate for detection of SCC in gas transmission pipelines [18].

CHAPTER 2. RESEARCH OBJECTIVES

2.1. Problem statement

The MFL method of in-line inspection currently used is not capable of detecting axially oriented SCC. A number of possible detection methods both electromagnetic and ultrasonic have been proposed and are being evaluated. The objective of this research is to develop and evaluate the feasibility of in-line inspection technology based on the remote field eddy current effect, using rotating magnetic field as an excitation.

In order to accomplish this task first, a feasibility study is carried out, using a three-phase rotor as excitation source. The method is evaluated with SCC as well as other defect types. A parametric study is carried out to investigate the defect size and location, and sensor type.

A data acquisition tool capable of collecting data at speeds of up to 10 mph with a linear resolution of 0.001" on 14 channels is designed and developed. The tool can be mounted on a mobile platform. A test rig with an 8" diameter pipeline is constructed in which the tool operates.

2.2. Scope of the dissertation

Chapter 3 presents the theory of generation of rotating magnetic field using poly-phase electric sources. The conventional and remote field eddy current testing are also introduced. Chapter 4 describes the static test bed and a feasibility study of using the method in the detection of various kinds of defects. Experimental results obtained using the system are presented. In chapter 5 the requirements for a data acquisition system are presented and the system design is discussed in detail. The chapter contains simulation result of the

components of the acquisitions system. The overall design of the pull rig is presented in chapter 6.

Chapter 7 presents the conclusions and discusses the direction of the future work.

CHAPTER 3. THEORETICAL BACKGROUND

3.1. Conventional eddy-current testing

Electromagnetic induction is the physical basis for all eddy current nondestructive testing techniques, including the earliest equipment developed by Hughes in 1876 to detect differences in metal conductivity [20]. An alternating current expressed as:

$$i = I_M \sin \omega t \tag{1}$$

in the excitation coil produces an alternating magnetic field strength, a vector quantity governed by the Maxwell-Ampere law:

$$\oint_C \overline{H} \cdot dl = \int_S \overline{J} \cdot ds \tag{2}$$

where $\vec{J}$ is the vector current density in the excitation coil, and the assumption is made that the displacement current density is negligible at the eddy current coil frequencies used in NDT applications.

The magnetic field described by (8) interacts with any conducting material in the vicinity of the excitation coil and induces an electric field strength governed by the Maxwell-Faraday law:

$$\oint_C \overline{E} \cdot dl = -\int_S \overline{B} \cdot ds \tag{3}$$

where B is the magnetic flux density, whose relation to the magnetic field strength H is given by the materials constitutive equation:

$$B = \mu_0 \mu_r H \tag{4}$$

where μ_o and μ_r are the absolute and relative permeability. Eddy currents are created by the induced electric field in material with conductivity σ as in:

$$J = \sigma E \tag{5}$$

The induced currents create magnetic field governed by the Maxwell-Ampere law, which tend to oppose the alternating excitation coil field according to the Lenz's law. This field interaction couples the properties of the material back into the excitation coil and affect its' impedance. The excitation coil voltage leads the current and can be expressed as in:

$$v(t) = V_M \sin(\omega t + \theta) \tag{6}$$

where θ is the phase angle. The impedance of the excitation coil can then be expressed as:

$$\bar{z} = \frac{\bar{v}}{\bar{i}} = \frac{1}{\sqrt{R^2 + X_L^2}\tan\frac{X_L}{R}} \tag{7}$$

where V and I are the phasor versions of the excitation coil voltage and current and R and X_L are the excitation coil resistance and inductive resistance.

Eddy current probes operate on the principle of electromagnetic induction. Material properties, including those caused by flaws and other inhomogenities can be detected by monitoring the steady state AC impedance of the probe coil as it passes over the area of interest in the test specimen.

The equations (2) - (4) are equivalent to the following elliptical diffusion equations [20]:

$$\nabla^2 H = j\omega\mu\sigma H \tag{8}$$

$$\nabla^2 E = j\omega\mu\sigma E \tag{9}$$

$$\nabla^2 J = j\omega\mu\sigma J \tag{10}$$

A solution of (10) in the idealized case of an infinite AC current sheet over a conducting half space is given by [21]:

$$\overline{J} = J_0 e^{\frac{-x}{\delta}} \sin(\omega t - \frac{x}{\delta}) \tag{11}$$

$$\delta = \frac{1}{\sqrt{\pi f \omega \mu}} \tag{12}$$

where J_0 is the current density at the surface of the half space and δ is the skin depth of penetration, or the depth at which J is 36.8% of J_0 and lags it by 1 radian. This definition for skin depth is for an idealized case, but the effect does limit the application of conventional eddy current testing methods to the detection of near surface defects. This limitation of the conventional eddy current method precludes its application in detecting SCC, since the cracks occur on the outside of a pipeline, whereas the inspection is done from the inside.

3.2. Remote field eddy current

In conventional eddy current testing the change in the impedance of the sensor coil is used to indicate the presence of material defects. Usually the exciting and sensing coil are the same and are normally operating between 1 KHz and 10 MHz. In remote field eddy current testing the exciter and the sensor coils are several pipe diameters apart and the frequency of operation is from 10 Hz to 160 Hz [22]. The probe does not measure the change in the impedance of the sensor coil; instead it measures the steady state AC phase angle difference between the exciter and the sensor coil. The skin effect restricts the conventional eddy current testing to near-surface defects, whereas the RFEC overcomes this limitation due to its sensitivity to both inner and outer diameter defects [23].

The RFEC effect was first observed in a situation where alternating current was applied to a coil inside a metallic pipe as shown in figure 3.1. The RFEC phenomenon is a process where the energy released from the excitation coil intersects the pipe wall twice before it reaches the pick-up coil. The pick-up coil is located several pipe diameters away from the excitation coil. This technique is now routinely used for inspection of metallic tubes due to its sensitivity to both ID and OD defects [24].

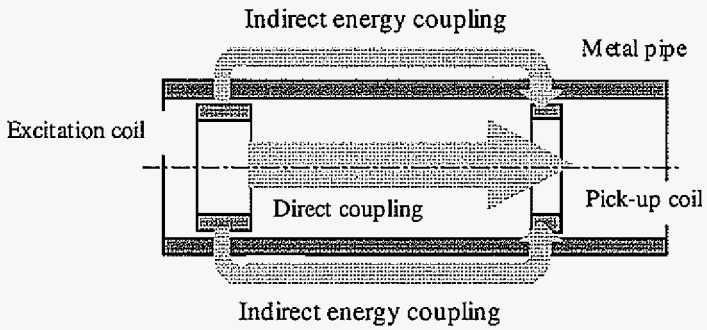

Figure 3.1. Remote field eddy current energy flow paths

Figure 3.2 shows the characteristics of the RFEC phenomenon. The magnitude and the phase angle of the pick-up coil signal are plotted against the distance (measured in pipe diameters) between the excitation and pick-up coils. There are three distinct regions: near field, transitional field and remote field. In the near field the magnitude of the signal decreases exponentially, whereas in the remote field the attenuation rate is much lower. The phase in the near field is close to –90°. In the remote field region the phase angle is a constant value different from that measured in the near field. The phase difference is approximately proportional to the pipe wall thickness. The transitional field is characterized with a rapid change in the phase angle and the magnitude attenuation rate.

The exponential attenuation of the signal in the near field is caused by the presence of the induced eddy currents in the tube wall. The phase value follows from Faraday's law, according to which the voltage of the eddy current pick-up coil is given by the relationship:

$$v(t) = -\frac{\partial \Phi}{\partial t} = -j\omega LI \qquad (13)$$

In other words, because of the inductive nature of the effect the induced voltage leads the excitation current by 90°. The relationship between the phase difference and the tube wall condition follows from the fact that the energy that reaches the pick-up coil, located in the remote field arrives primarily via the indirect path. The energy released from the excitation coil crosses the tube wall twice, from inside to outside in the near field and from the outside to the inside in the remote field. This complex path explains the dependence of the phase angle on the tube wall conditions.

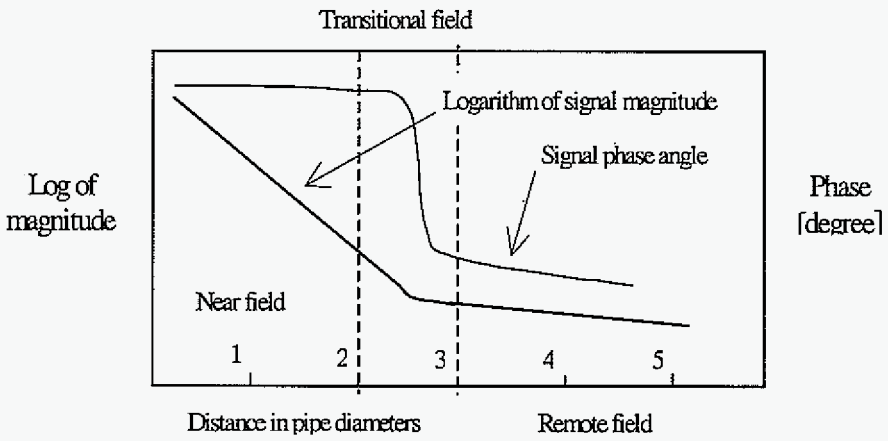

Figure 3.2. Remote field eddy current signal magnitude and phase

Finite element simulations of the RFEC phenomenon indicate that in the transitional field the RMS magnetic vector potential magnitude and phase exhibit "potential valley" and "potential knot", or areas where the RMS magnetic vector potential magnitude is zero and phase angle is undetermined. The transitional field is observed at a distance of one to two tube diameters from the excitation coil.

CHAPTER 4. STATIC TEST BED RESULTS

The RFEC technique is routinely used for the detection of both ID and OD defects in pipes. A static test bed was built in order to evaluate the feasibility of using RFEC for the detection of SCC. A test specimen containing a colony of SCC and a set of defects machined on the outer surface was used in this feasibility study.

4.1. Static test bed

An 8" steel pipe is used as a test specimen. The pipe has an SCC colony on the external surface. The SCC colony is clearly visible on the photograph shown in figure 4.1. The colony is sparse with a length of approximately 2". In addition to the colony a set of axially oriented defects were machined on the outer surface. The defects are saw-cuts with depths of 20%, 40%, 60% and 80% of the wall thickness. All defects are 25.4 mm long and 0.38 mm wide.

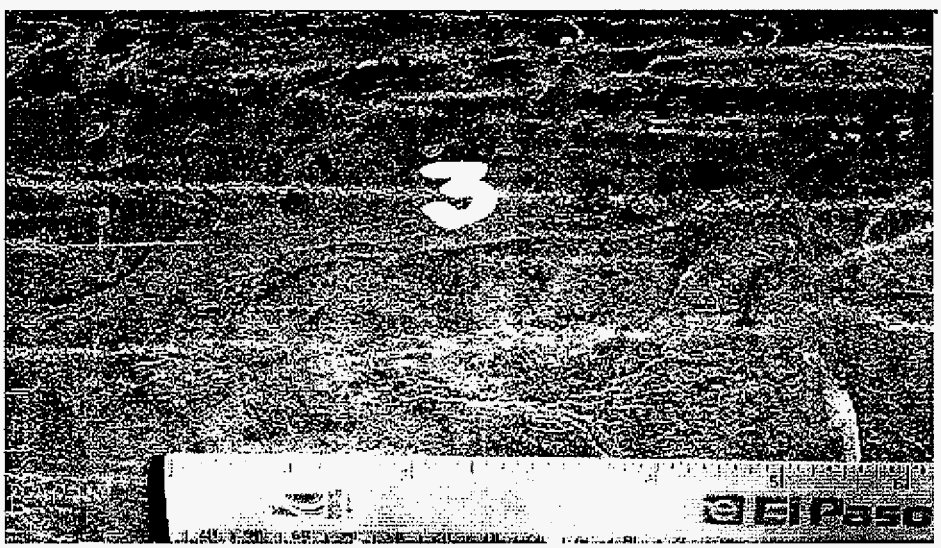

Figure 4.1. SCC colony

Figure 4.2 shows a schematic of the static test bed. A three-phase, 8" diameter rotor is used as an excitation source powered by a three-phase power supply, set at 33 Hz. The power supply used was "Invertron", Model 251T from California Instruments. The rotor is mounted on roller-blade wheels, which allows it to be located easily anywhere inside the test pipe. Special care is taken to ensure that the rotor is centered in the pipe and oriented along the pipe axis. The system uses a computer-controlled scanner, which allows the sensor to be rotated along the circumference of the test pipe, with accuracy of 0.9° and along the pipe axis, with an accuracy of quarter inch. The scanner is build from two Arrick Robotics stepper motors powered by a stepper motor controller model MD2, supplied by the same company. Both motors use either 1:2 or 1:4 gear reducers. The reducers were necessary to overcome the friction between the sensor housing and the pipe surface and in order to increase the positioning accuracy.

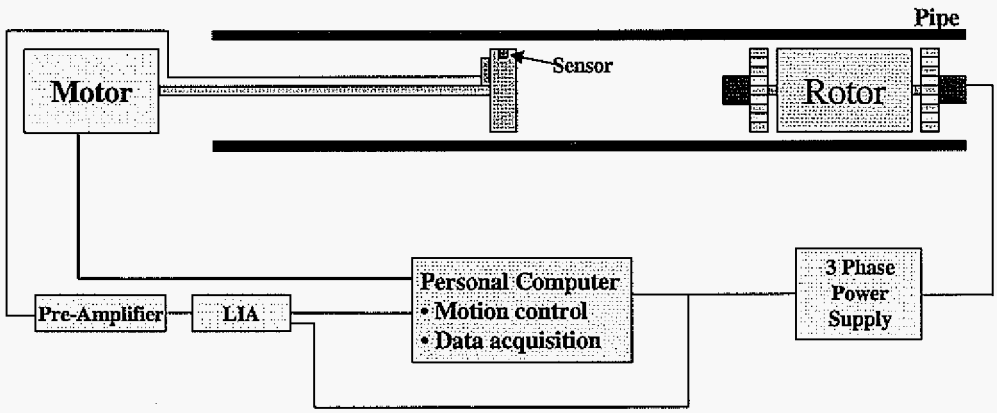

Figure 4.2. Schematic of the static test bed

4.2. Sensor design

An E-shaped core with a coil on the middle leg is used as a sensor. A 3D drawing of the sensor is shown in figure 4.3. Such placement of the coil is critical, because it allows a

differential measurement of magnetic flux. This can be explained by considering the flux paths in the circuits composed of the middle and left legs on one hand and the middle and right leg on the other. The magnetic flux in these two circuits is oriented such that the common component cancels out in the middle leg (as long as the defect is located above the middle leg of the sensor as in figure 4.4. a). Figure 4.4 b) illustrates another configuration, in which the sensor does not produce differential signal. In it the defect is oriented perpendicularly to the axis of the sensor.

The sensor is mounted in a protective plastic enclosure and is secured in the scanner disk. The sensor output is coupled to a 40dB pre-amplifier build from an LT 1069 gain-programmable operational amplifier. The pre-amplifier output is fed to an ITHACO lock-in amplifier model 3981, which is used to measure the phase and magnitude of the voltage induced in the coil. The lock-in amplifier is computer-controlled and the PC handles the data acquisition and display.

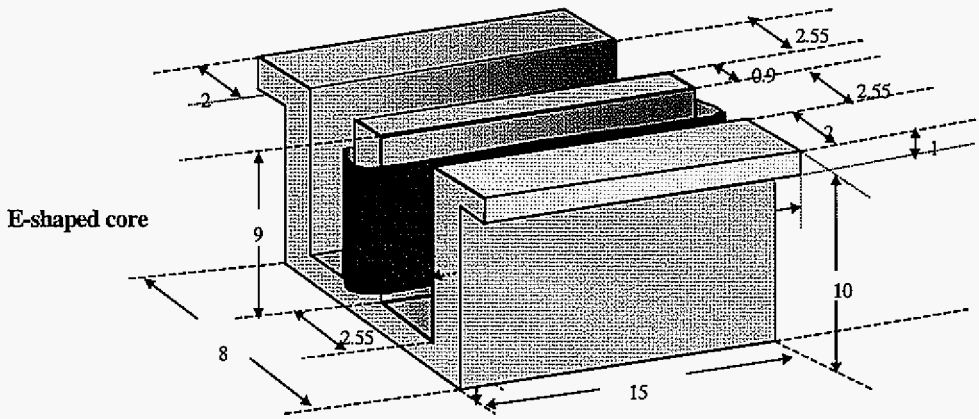

Figure 4.3. Static test bed sensor

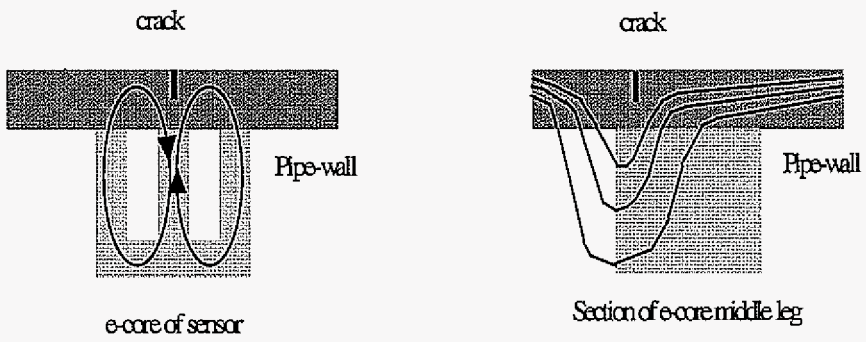

a) b)

Figure 4.4. Sensor in differential configuration (a) and absolute configuration (b)

4.3. Measurement results for axially oriented saw-cut defects

RFEC method relies on the sensitivity of the pick-up coil located in the remote field to OD defects. Generally it is thought that the remote field starts some two to three pipe diameters away from the excitation source. Before any measurements of defect signals are done, the distance at which the remote field region is located has to be found. This is done by measuring the magnitude of the voltage induced in a coil as it scans the ID and OD surfaces of a defect-free pipe. The result of this measurement is shown on figure 4.5. The arrow indicates the position at which the remote field region starts. This is the position in the pipe at which the energy of the indirect coupling path dominates the energy in the direct coupling path (see figure 3.2). It was found that for this set-up measurements should be done at least 39" away from the excitation rotor center.

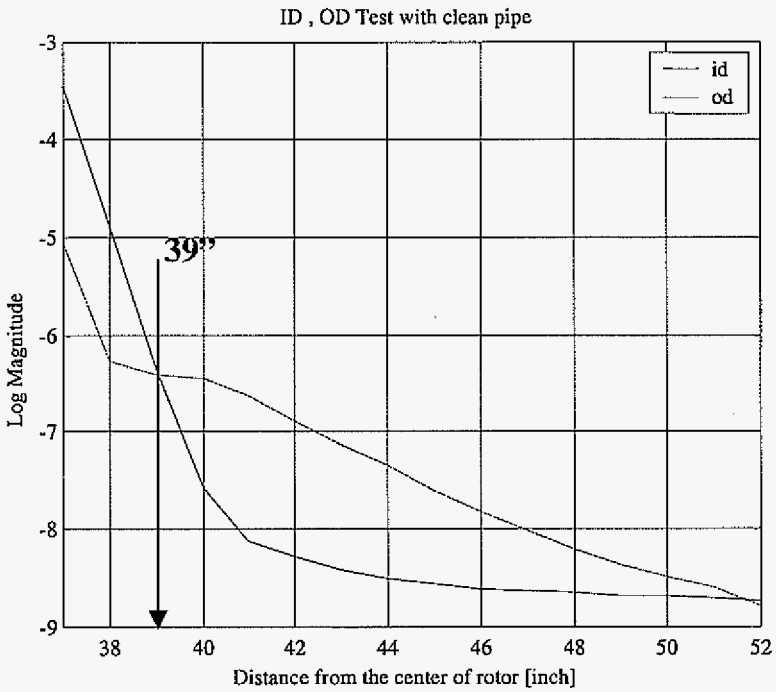

Figure 4.5. ID, OD tests on defect free pipe

The following figures 4.6 through 4.9 show the results from the tests done on the ID side of the test pipe under 80, 60, 40 and 20 % deep saw cuts. The saw cuts were produced using a circular saw and their depth is constant.

The plots show a spatial derivative of the wavelet de-noised signal of the phase of the coil voltage measured with respect to one of the rotor windings. The peak in the middle of the 2-D scan represents the defect signal. The signals obtained for the 80% through 40% deep defects are very pronounced. Wavelet de-noising was necessary to enhance the weakest signal, obtained from the 20% deep defect.

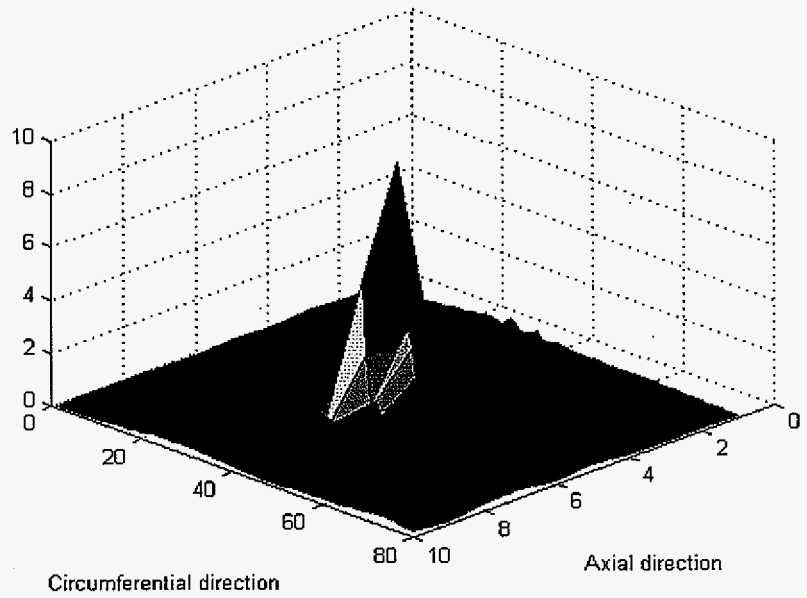

Figure 4.6. Phase measurements obtained from a 2-D scan of an 80% deep saw-cut

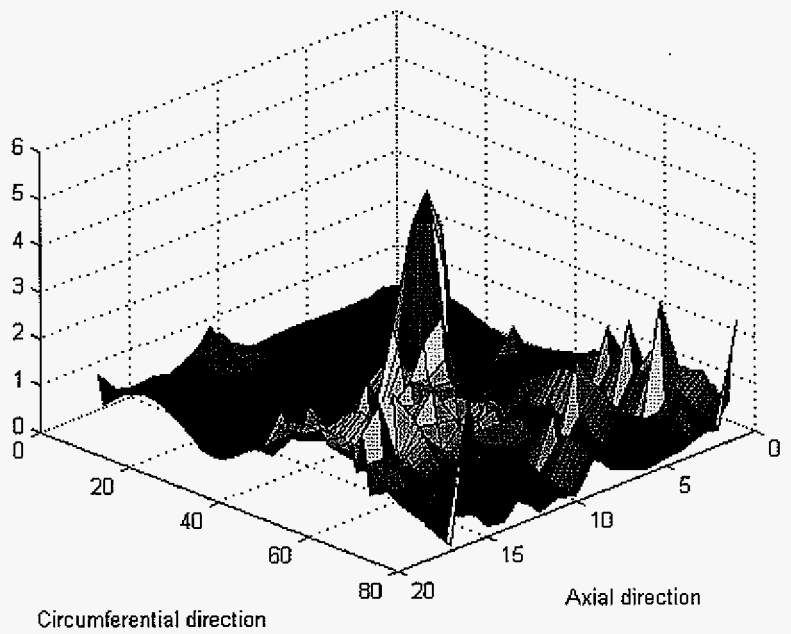

Figure 4.7. Phase measurements obtained from a 2-D scan of a 60% deep saw-cut

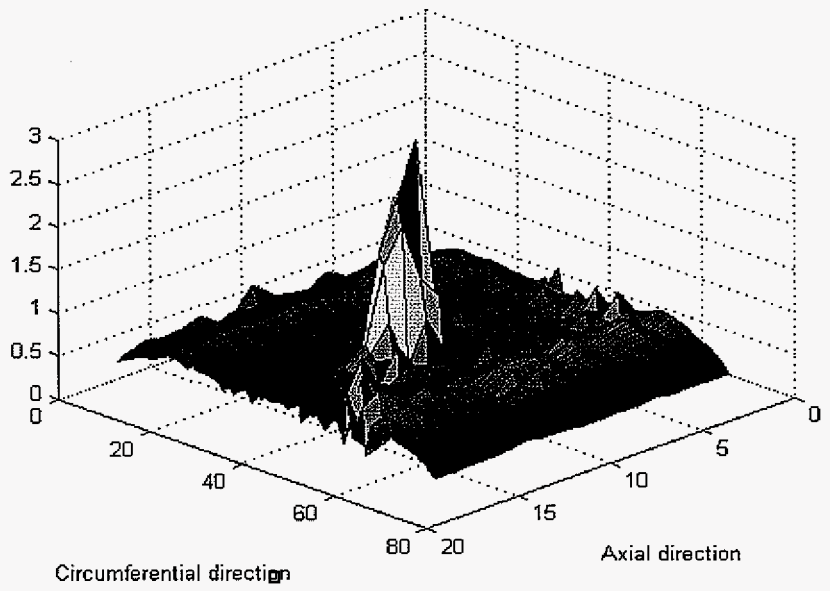

Figure 4.8. Phase measurements obtained from a 2-D scan of a 40% deep saw-cut

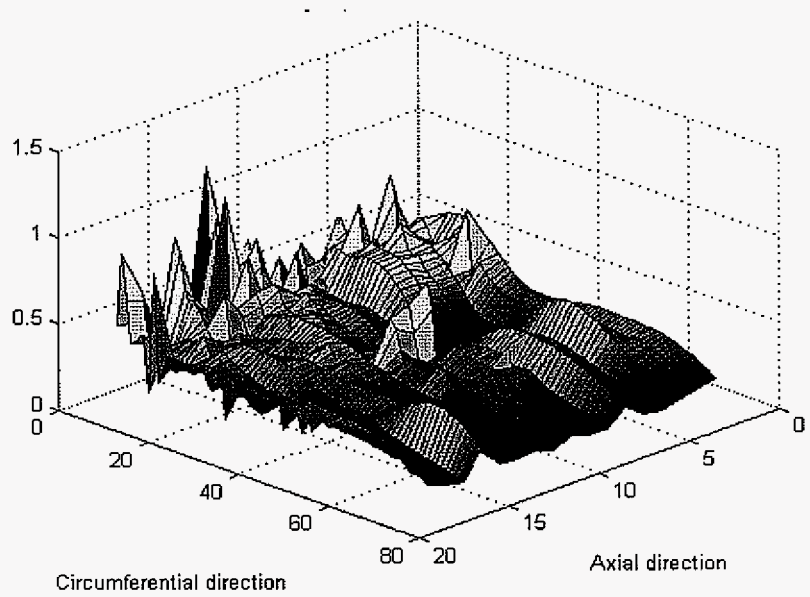

Figure 4.9. Phase measurements obtained from a 2-D scan of a 20% deep saw-cut

4.4.Measurement results for SCC colony

Figure 4.10 shows the results from the experimental measurements on the ID side of the test pipe under the colony of SCC. The plot shows of the phase of the coil voltage with respect to that of one of the rotor windings.

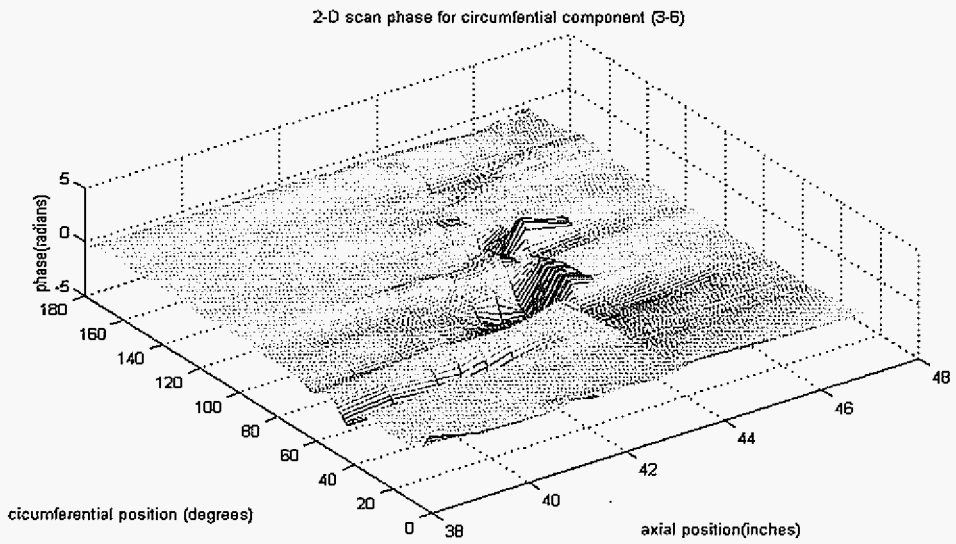

Figure 4.10. Phase measurements obtained from a 2-D scan of an SCC colony

4.5. Discussion of test results for axially oriented defects and SCC

The results obtained from the static test bed suggest that the RFEC method is a good candidate for detecting axially oriented flaws. All of the defects produced measurable signals. As explained earlier the phase of the signal contains information about the presence of a defect. It has to be noted however that the saw-cut is a much larger defect. SCCs are very tight compared to a saw-cut. In addition to this, SCCs contain oxide and other materials that can be conductive, whereas saw-cuts are "clean" i.e. current cannot flow through the faces of the cut.

Nevertheless the measurement result from the SCC colony is very encouraging. The SCC produces a large footprint and the signal level is sufficient to detect. However, nothing is known about the depth of the SCC. Additional difficulty would be to replicate these results on the mobile platform. It is not clear what effect the velocity of the tool will have on the signal, but it could be expected that it would decrease the signal strength. These questions can only be answered once the test rig is build and tested. In order to investigate the effect of tool velocity a parametric study should be carried out, where test conditions such as: defect type, sensor placement, excitation power and frequency, should remain unchanged, while the velocity of the tool is varied.

4.6.Static test bed results obtained for circumferentially oriented notches, skewed notches and round defects

The results shown in the previous sections demonstrated that the RMF-RFEC technique can be used successfully to detect axially oriented flaws. This section discusses the possibility of using the technique in detection of other types of defects: circumferentially oriented notches, skewed notches (notches occurring at an angle to the pipe axis) and round defects (pits). While SCC do not occur along the circumference some skewed SCC have been found in practice, particularly at bent sections of a pipeline. Round defects can be used to simulate corrosion pits, and the larger they are in diameter, the more difficult they are to detect.

Two defect sets were used in the measurements discussed in this section. These are described below:

- a set of four circumferentially oriented saw-cuts with maximum depths of 20%, 40%, 60% and 80% of the pipe-wall;
- a set of four skewed (approximately 45 degrees to the pipe axis) saw-cuts with maximum depths of 20%, 40%, 60% and 80% of the pipe-wall;
- a set of three round defects, 1.0" diameter with a depth of 20% and 30% of the pipe wall and a 1.5" diameter round pit with a depth of 20% of the pipe-wall;

All saw-cuts were produced using a hand-held hacksaw on a 8" ID steel pipe. During cutting the depth of the defect was constantly monitored, as soon as the desired depth was reached in one spot the cutting was stopped. The cuts have therefore irregular dimensions, the deeper a defect is the greater its length becomes, since it is cut on a cylindrical surface. All the round defects were produced in one 8" ID steel pipe section, using a grinding wheel attached to a drill press. As with the saw-cuts, the depth was constantly monitored and grinding was stopped as soon as a desired depth is reached in one spot. As a result of this the defects have irregular depth and shape (in the case of the 1.5" diameter defect).

The orientation of the sensor with respect to the direction of the defect determines if the measurement is differential in nature. When the sensor axis co-insides with the axis of the observed defect a differential measurement is possible as illustrated on figure 4.4. This was the case with the axially oriented defects. Circumferential orientation of the defect therefore requires that the sensor be oriented in circumferential direction, when scanning the ID surface. The set of defects contains saw-cuts oriented at an angle to the pipe axis, as well as round shaped defects. It is clear that the orientation of the sensor is very important. In order to study the effect of the sensor orientation two sets of measurements were obtained for each of the defects, one with the sensor oriented along the pipe axis and another with the sensor oriented in circumferential direction. However, the sensor is specifically designed to be oriented along the pipe axis and when oriented along the circumference it does not have the same coupling.

Another important measurement parameter is the axial step of the scanner. If the step is too great, for example 1" or 0.5" the defect signal can be missed, since the RFEC phenomenon is highly localized. It was found that a step of 0.25" allows the observation of defect signals, but steps of 0.125" and 0.065" were also used. It would seem that the step should be as small as possible, to achieve high resolution. However, this is not the case, due to the existing friction between the sensor and pipe wall. Using a very small axial step results in a very unreliable measurement – the sensor is practically "stuck" at one position and then it "jumps" to a position two or more steps away.

Figures 4.11 through 4.14 show the magnitude and phase of the coil signal measured under a set of 20%, 40%, 60% and 80% deep circumferential saw-cuts, with the sensor oriented in axial direction (i.e. the sensor axis is perpendicular to the axis of the defect). Figures 4.15 through 4.18 show the magnitude and phase of the coil signal measured under a set of 20%, 40%, 60% and 80% deep skewed saw-cuts, with the sensor oriented in axial direction (i.e. the sensor axis is oriented at approximately 45 degrees to the axis of the defect). Figures 4.19 through 4.21 show the magnitude and phase of the coil signal measured under a set of 20% deep 1.0" round defect, 20% deep 1.5" round defect and 30% deep 1.0" round defect, with the sensor oriented in axial direction.

Figures 4.22 through 4.25 show the magnitude and phase of the coil signal measured under a set of 20%, 40%, 60% and 80% deep circumferential saw-cuts, with the sensor oriented in circumferential direction (i.e. the sensor axis is parallel to the axis of the defect). Figures 4.26 through 4.29 show the magnitude and phase of the coil signal measured under a set of 20%, 40%, 60% and 80% deep skewed saw-cuts, with the sensor oriented in circumferential direction (i.e. the sensor axis is oriented at approximately 45 degrees to the axis of the defect). Figures 4.30 through 4.32 show the magnitude and phase of the coil signal measured under a set of 20% deep 1.0" round defect, 20% deep 1.5" round defect and 30% deep 1.0" round defect, with the sensor oriented in circumferential direction.

An arrow on each of the plots indicates the position of the defect related signal. The plots present unprocessed data, therefore they contain some noise. All sharp peaks are a result of a measurement error. The data presented in figures 4.11 through 4.14 indicate that 40%, 60%, 80% deep circumferentially oriented notches can be detected by an axially oriented sensor, while the 20% saw-cut would be missed. Also, the presence of defects is detected from the magnitude plot, rather than phase plot. Figures 4.15 through 4.18 suggest that an axially oriented sensor can detect all the skewed saw-cuts. While the 20% deep cut can only be detected from the magnitude plot, all the other defects have both phase and magnitude signatures. Figures 4.19 through 4.21 show that the axially oriented sensor can detect all of the round defects. The presence of a defect is indicated by the peak-and-valley pattern on the magnitude plots. Only the 30% deep defect produced a phase signature.

The data presented in figures 4.22 through 4.25 indicates that a circumferentially oriented sensor can detect all the circumferentially oriented notches. The 20% saw-cut produced only a magnitude signature. The 40%, 60% and 80% deep defects have strong phase and magnitude signatures, with the 80% saw-cut producing stronger phase signal than magnitude signal. Figures 4.26 through 4.29 suggest that a circumferentially oriented sensor can detect all the skewed saw-cuts. While the 20% deep cut can only be detected from the magnitude signal, all the other defects can be detected from either the magnitude or the phase signal. Figures 4.30 through 4.32 show that the circumferentially oriented sensor can detect all of the round defects. The presence of a defect is indicated by the peak-and-valley pattern on the magnitude plots.

4.7. Discussion of the test results obtained for circumferentially oriented notches, skewed notches and round defects

The data presented in figures 4.11 through 4.32 indicate that circumferentially oriented notches, skewed notches and round defects could be detected using the RMF-RFEC method. In all but one cases the presence of a defect was detected. Circumferentially oriented flaws produced signatures in the magnitude of the signal, when axially oriented sensor was used (i.e. when the sensor axis was perpendicular to that of the defect) and both magnitude and phase signatures, when the sensor was oriented in circumferential direction (i.e. the sensor axis was parallel to that of the defect). This was not the case for the 20% deep defect, which was missed by the axially oriented sensor, but could be detected from the magnitude of the signal produced by a circumferentially oriented sensor.

Skewed saw-cuts produced a distinct pattern in both the magnitude and the phase of the signal measured with a sensor oriented in either axial of circumferential direction. An exception of this observation is the case of a 20% deep defect, which produced only a magnitude signature. Round defects produced a distinct peak-and-valley pattern in the magnitude of the signal measured with a sensor oriented in either circumferential or axial

direction. Only the 30% round flaw produced a phase signature, when the sensor was oriented in axial direction.

The magnitude of the sensor signal can be used to detect the presence of defects. This indicator has one problem – it is sensitive to lift-off. This may require additional signal processing to make the measurement lift-off invariant. Estimation of the phase of the measured signal is not affected by the sensor lift-off, provided that the signal level is sufficient to obtain the phase.

The RFEC method of inspection relies on the information found in the phase of the sensor signal rather than in its magnitude. However, the experimental results demonstrate that the signal magnitude is also affected by the presence of a defect. One possible explanation is that when the sensor axis is not parallel to the defect, the measurement is not differential and it registers the magnetic flux leakage (MFL), caused by the defect. An axially oriented sensor would then produce a typical MFL signature for a circumferentially oriented notch, or a round defect and only a phase signature for an axially oriented defect. Skewed defects would produce both magnitude and phase signatures. This observation suggests that the proposed method of inspection could be used to not only detect the presence of a defect, but to also characterize it in terms of its direction.

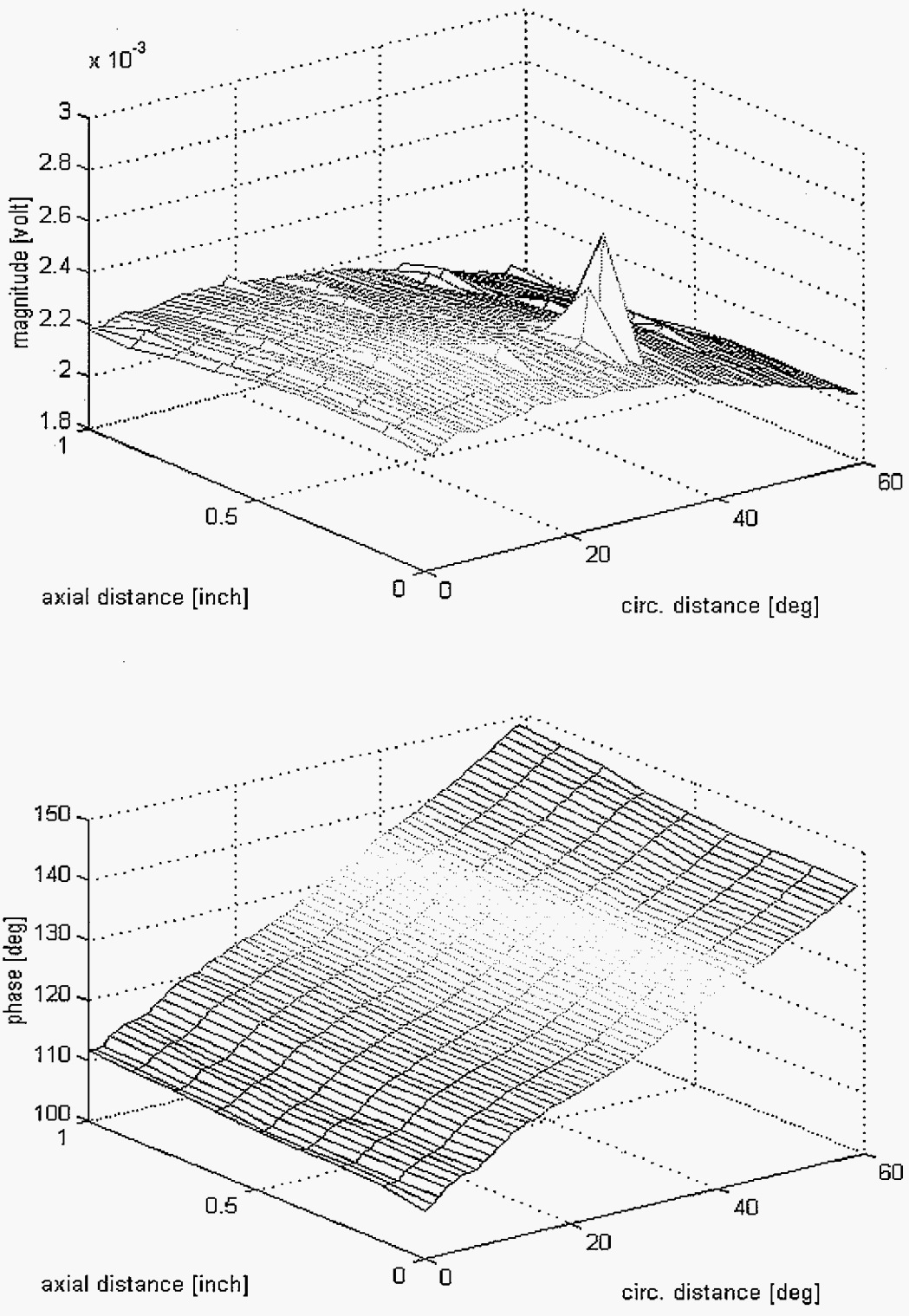

Figure 4.11. 20% deep circumferential notch signals

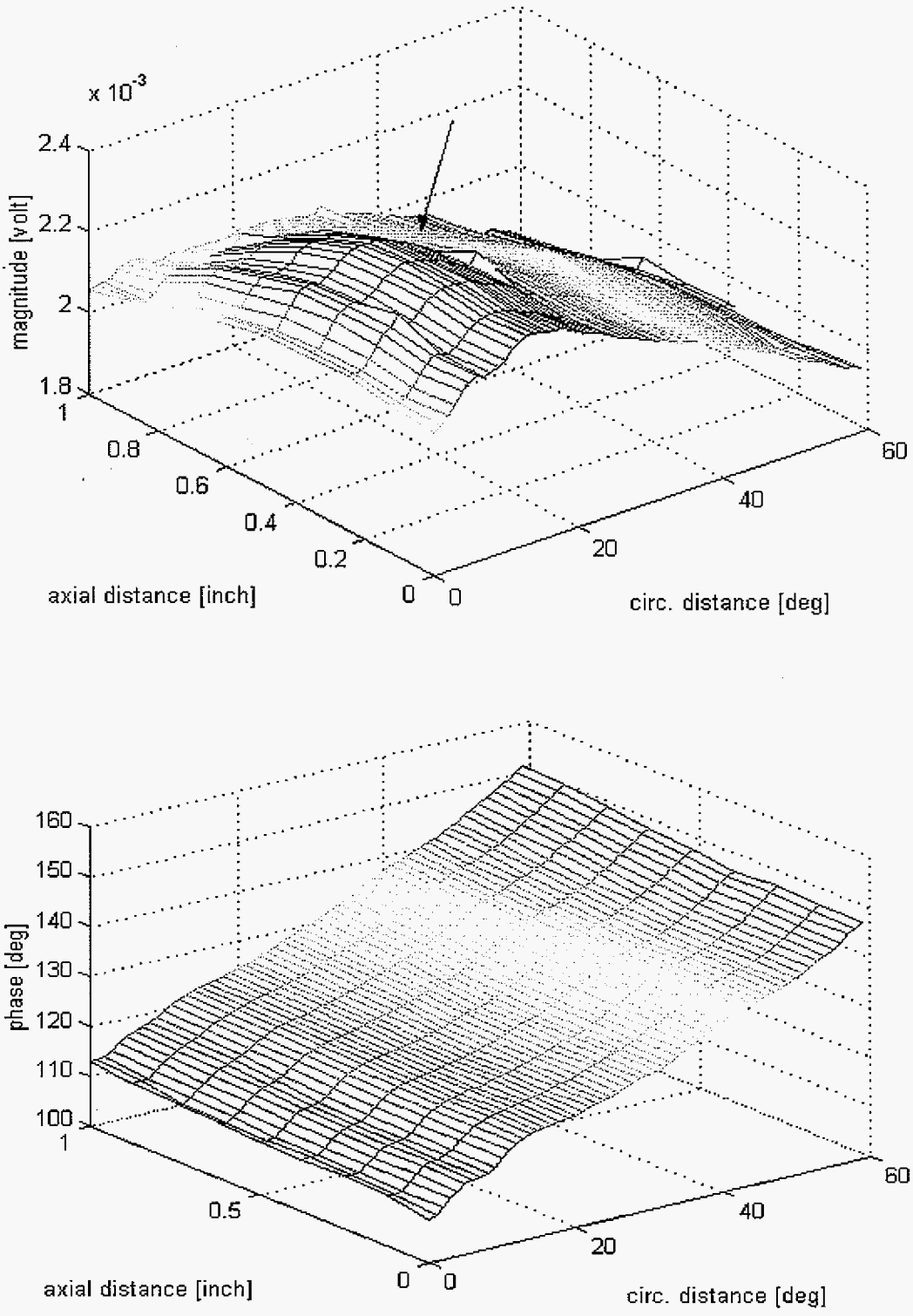

Figure 4.12. 40% deep circumferential notch signals

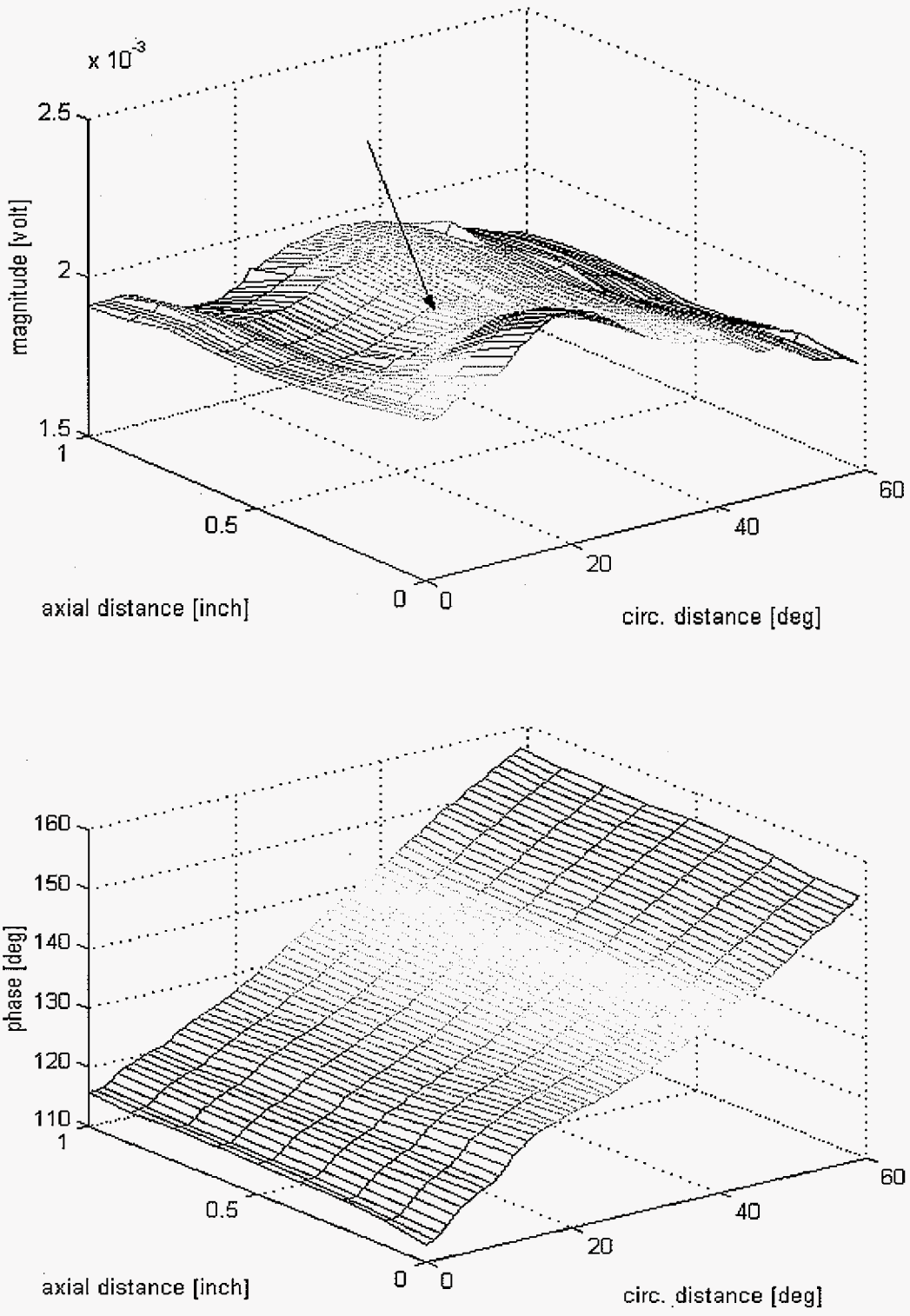

Figure 4.13. 60% deep circumferential notch signals

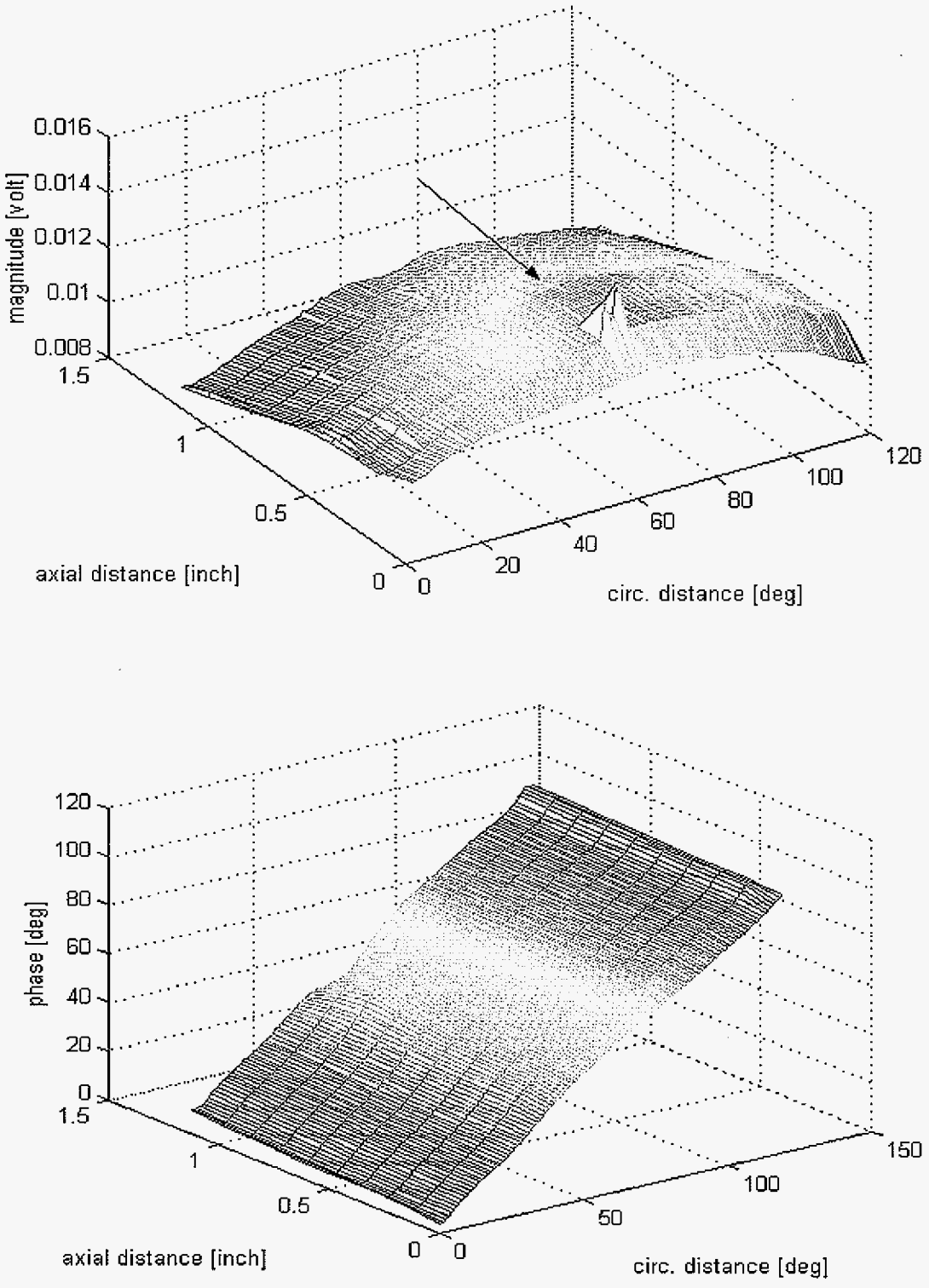

Figure 4.14. 80% deep circumferential notch signals

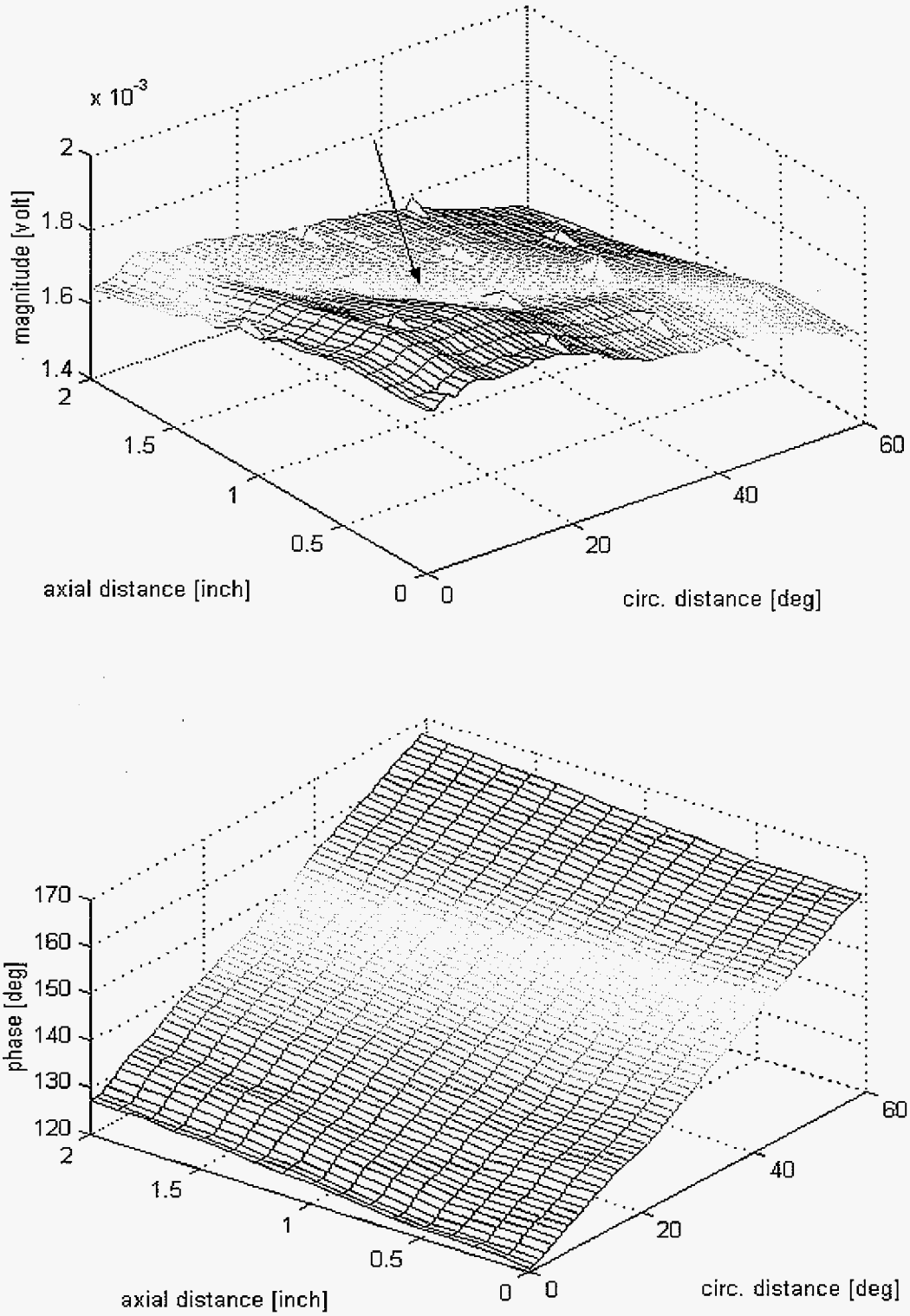

Figure 4.15. 20% deep skewed notch signals

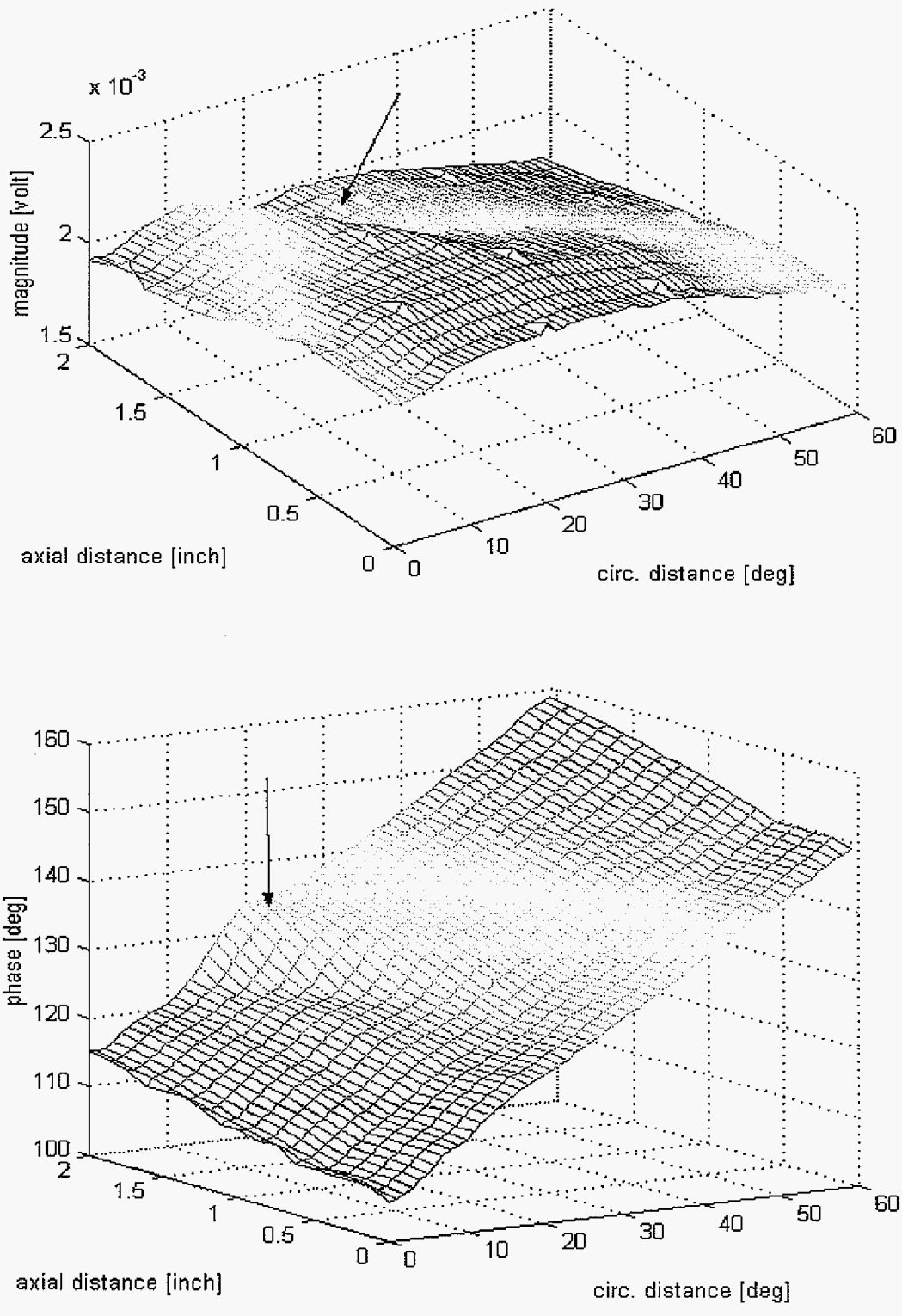

Figure 4.16. 40% deep skewed notch signals

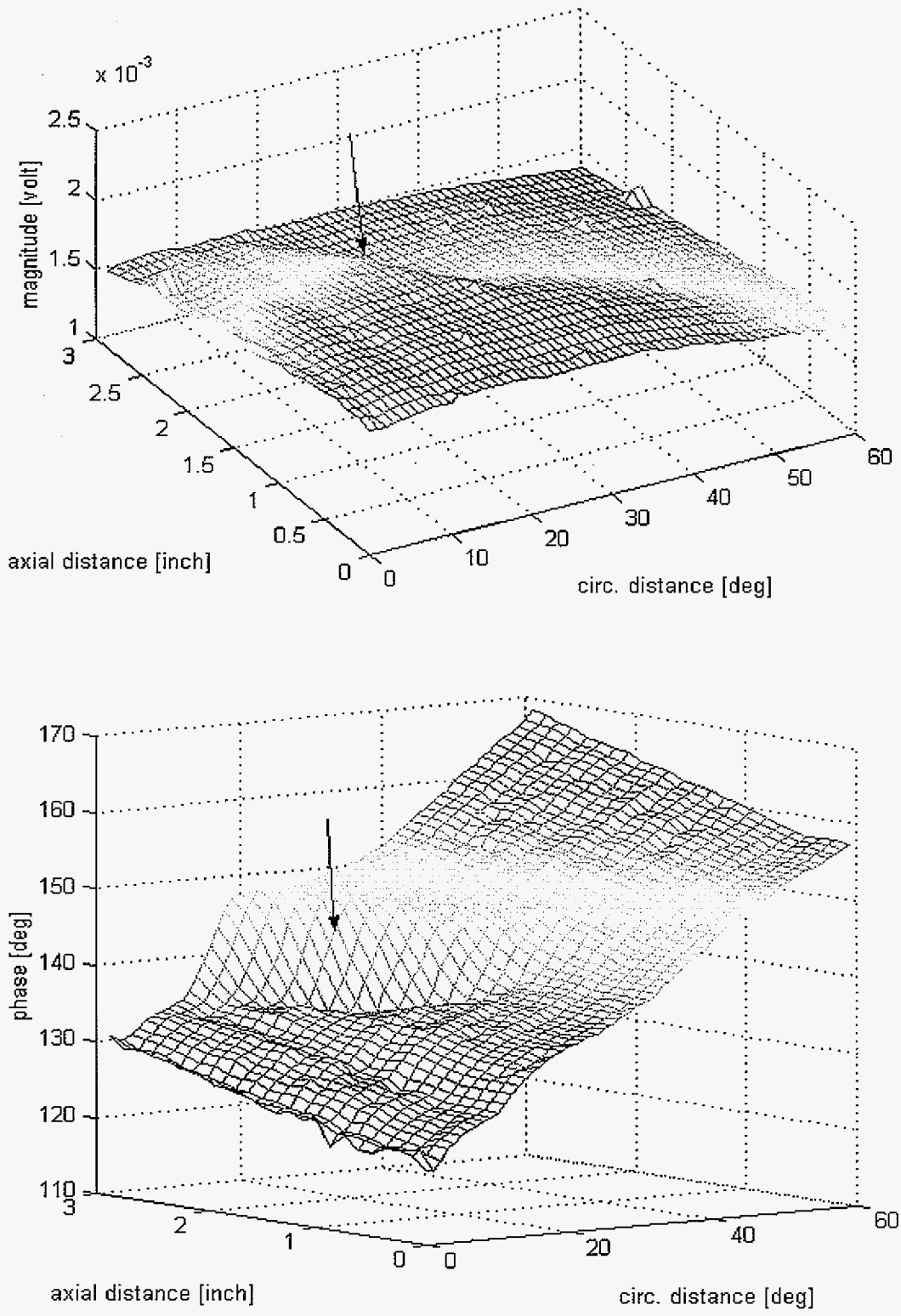

Figure 4.17. 60% deep skewed notch signals

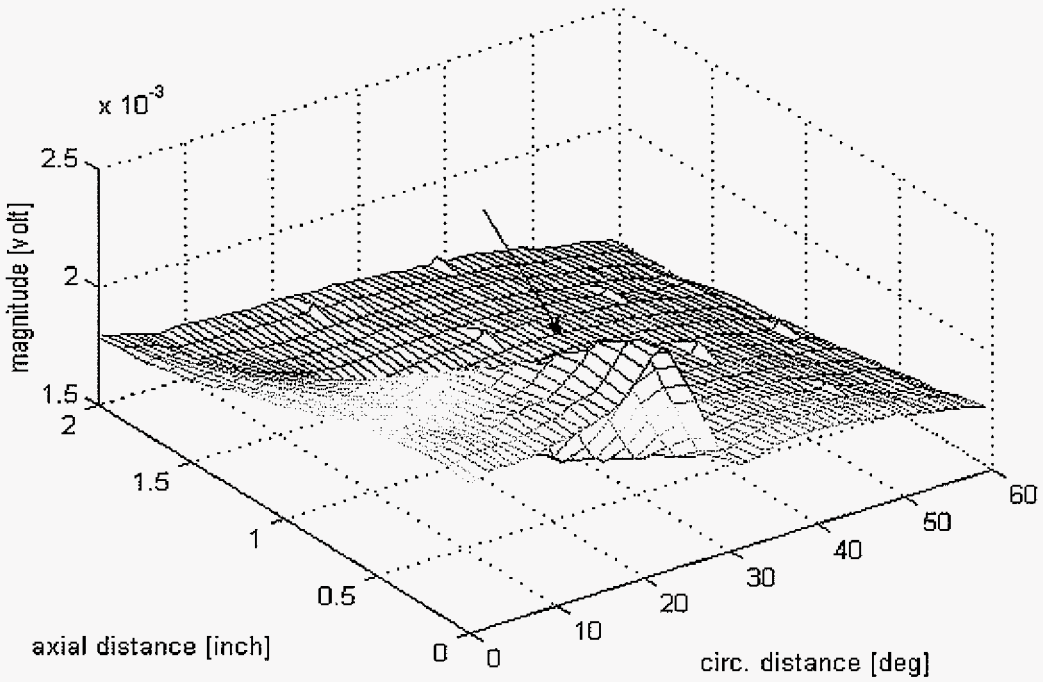

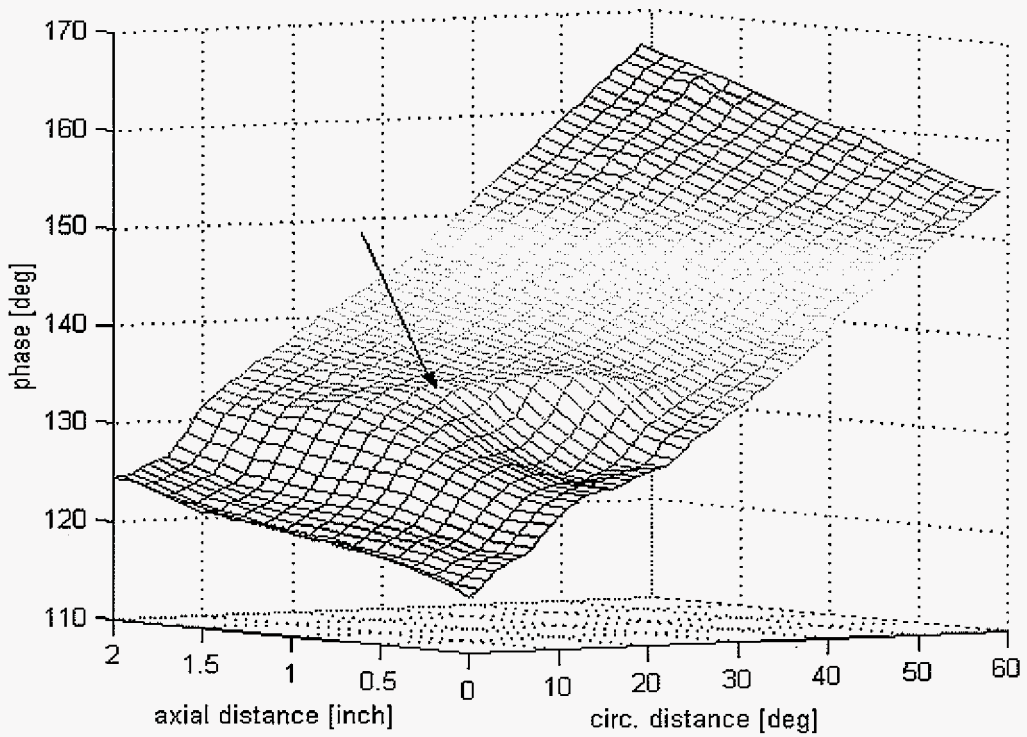

Figure 4.18. 80% deep skewed notch signals

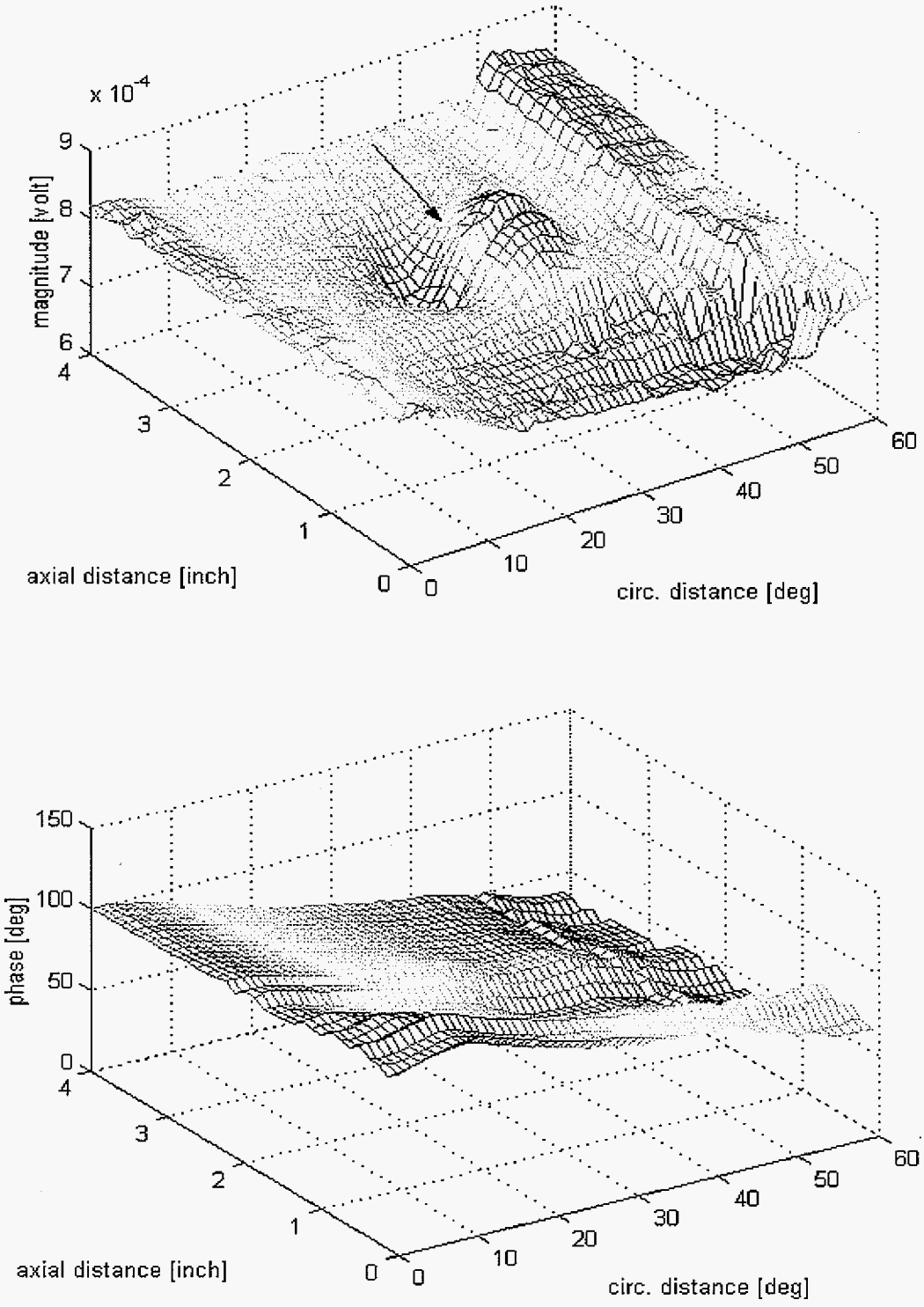

Figure 4.19. 20% deep 1.0" round defect signals

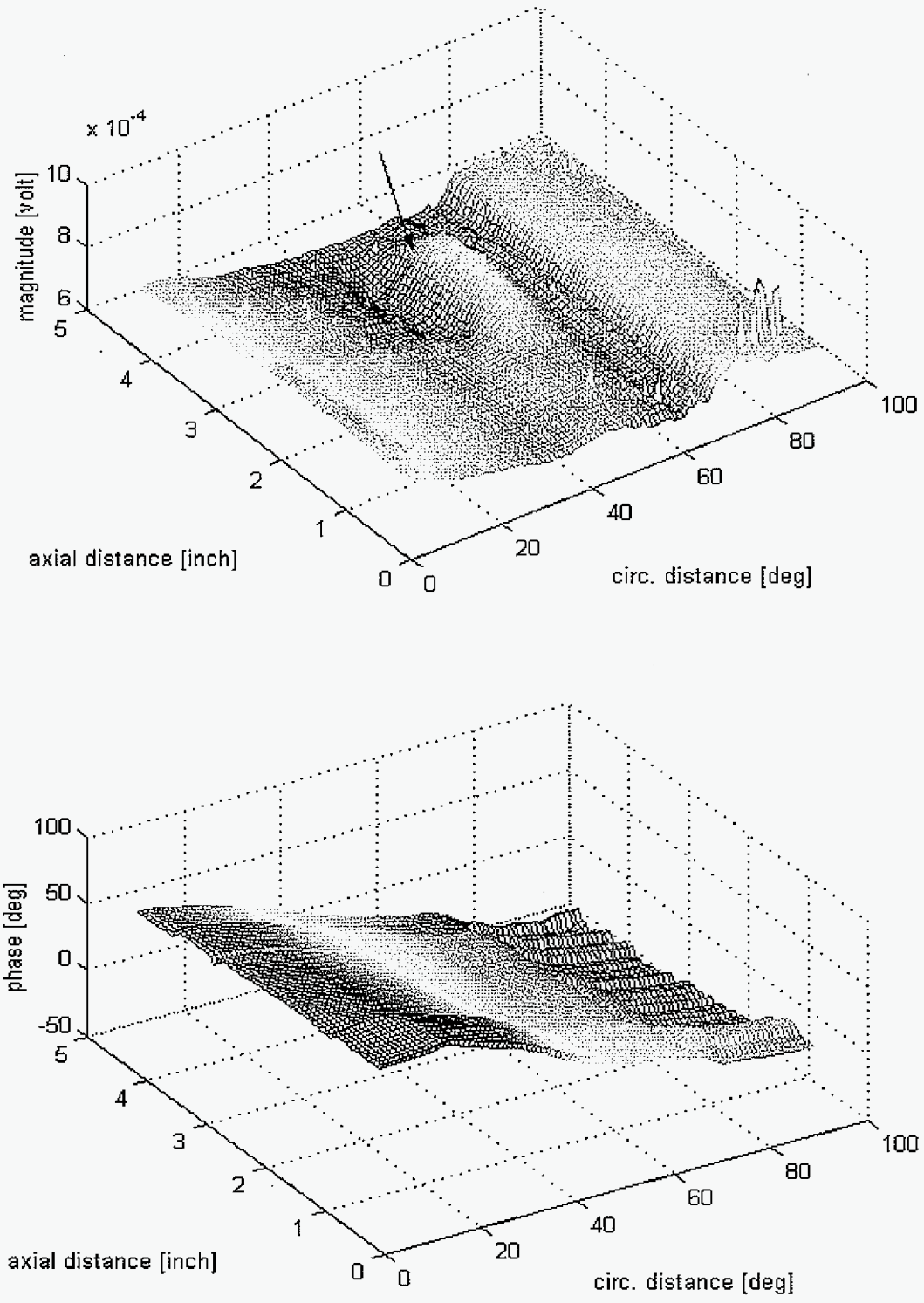

Figure 4.20. 20% deep 1.5" round defect signals

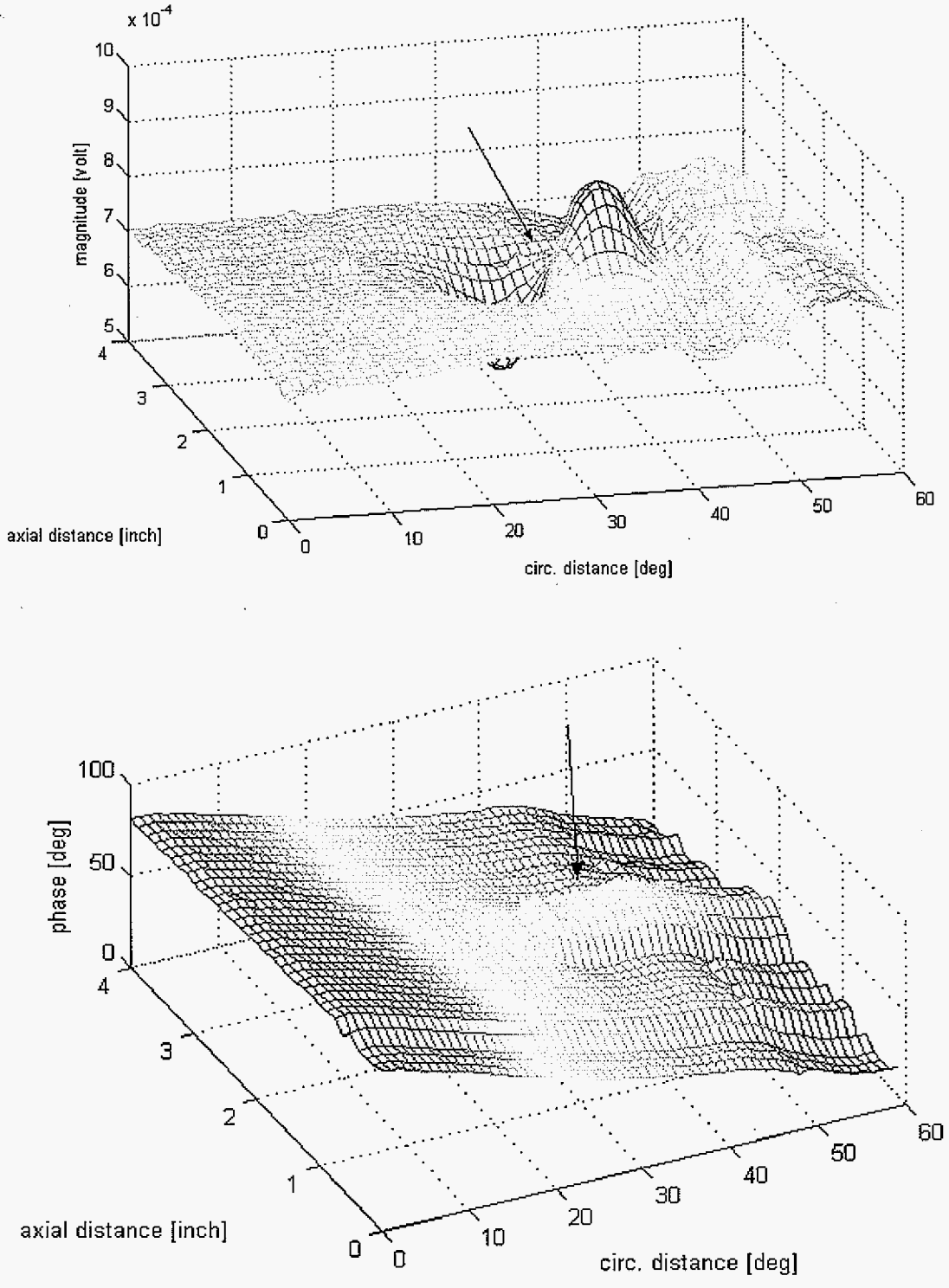

Figure 4.21. 30% deep 1.0" round defect signals

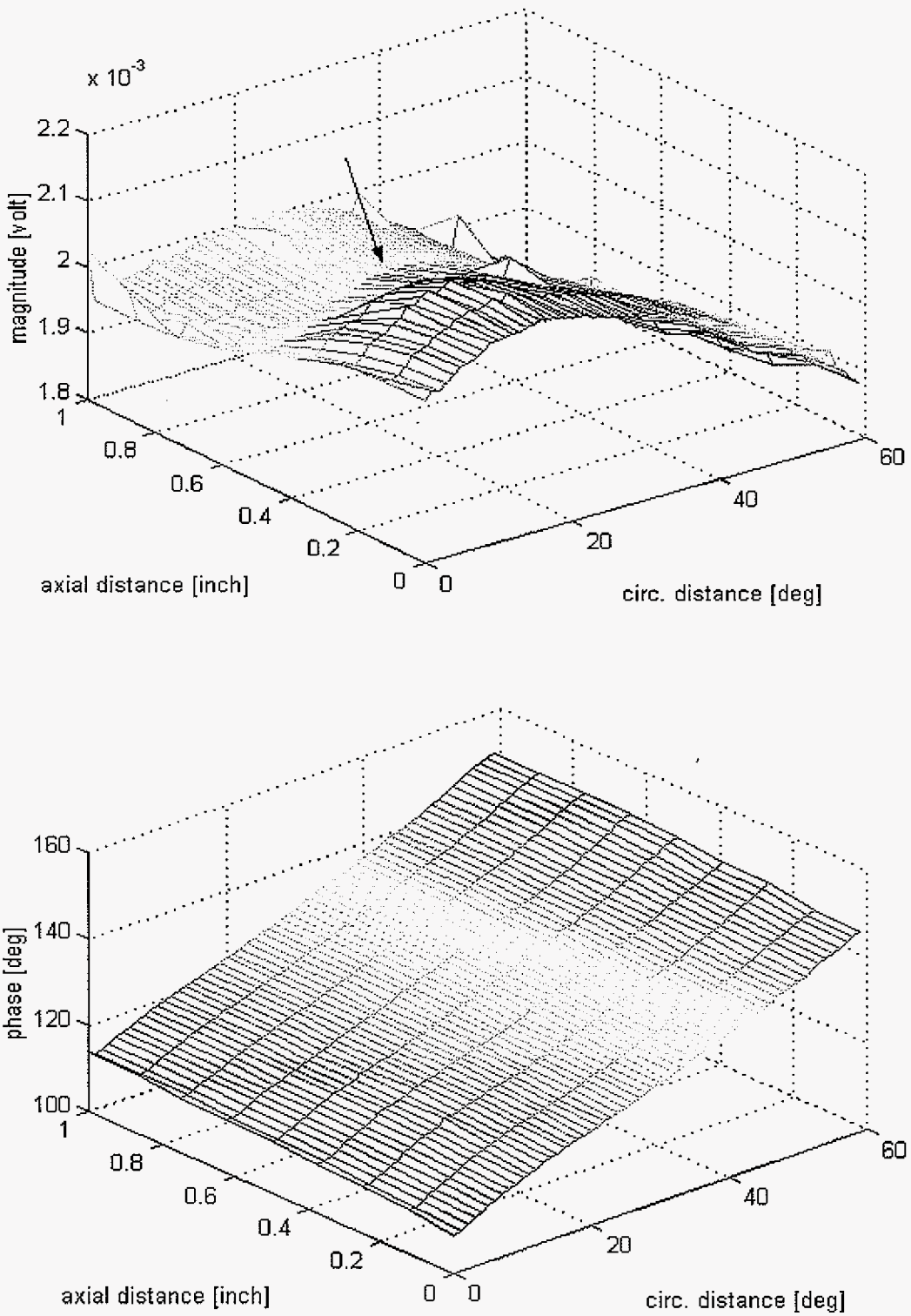

Figure 4.22. 20% deep circumferential notch signals

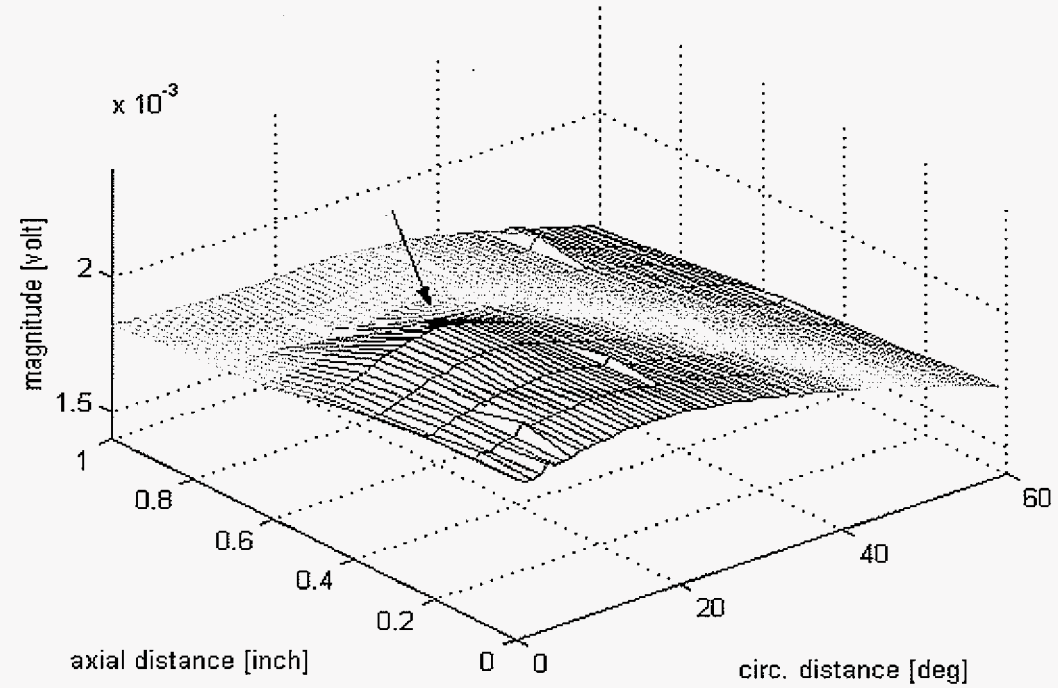

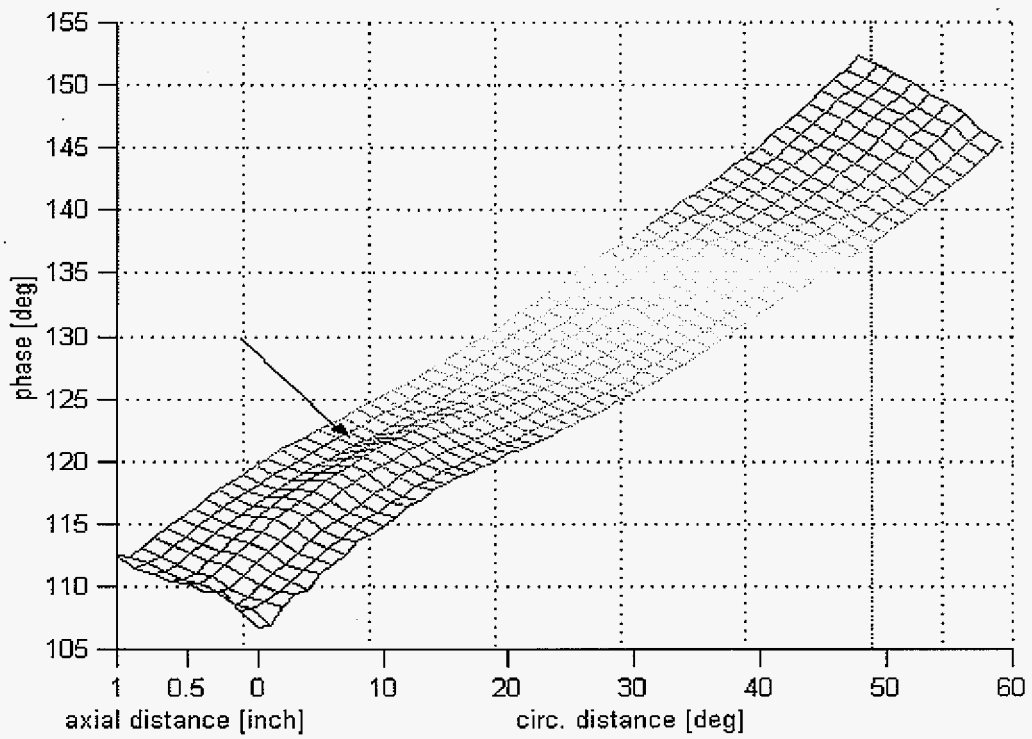

Figure 4.23. 40% deep circumferential notch signals

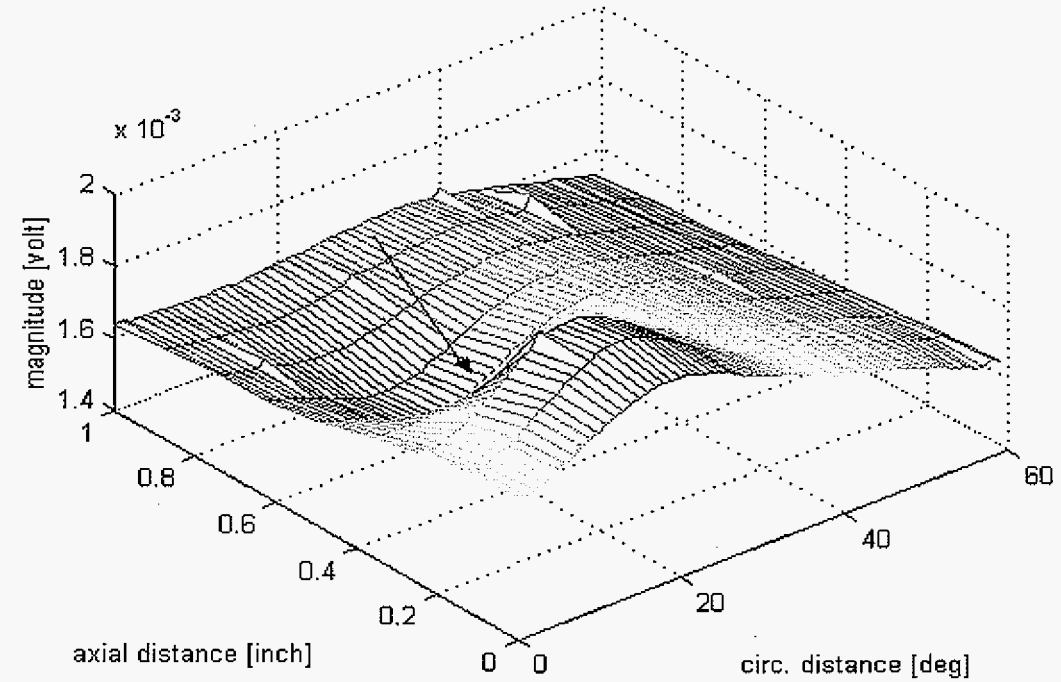

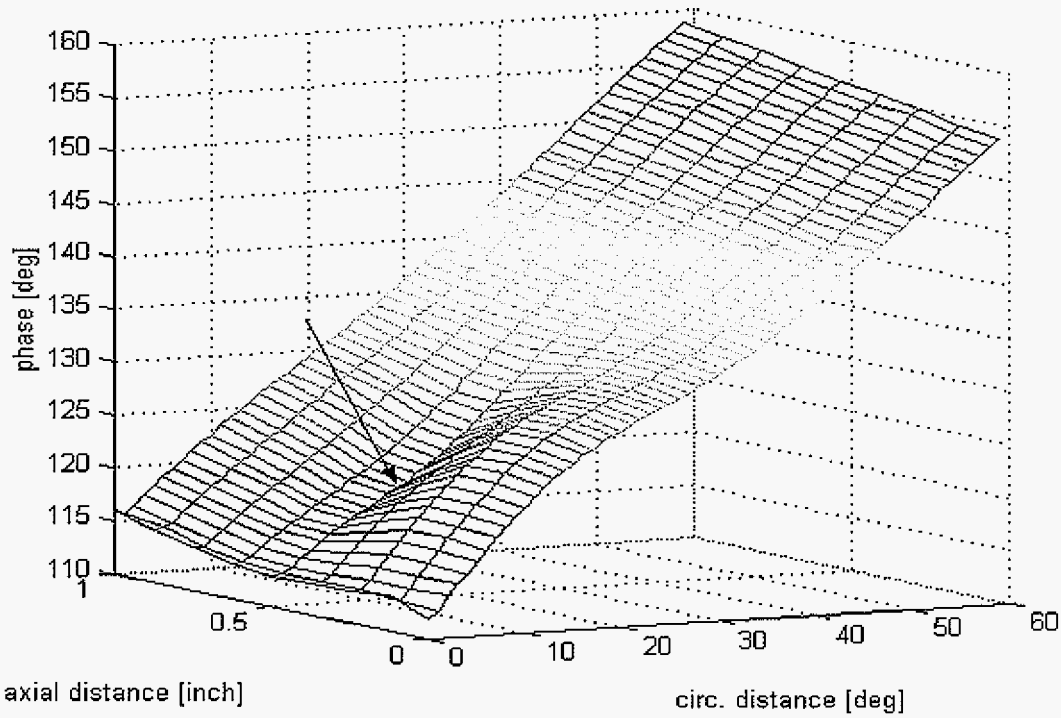

Figure 4.24. 60% deep circumferential notch signals

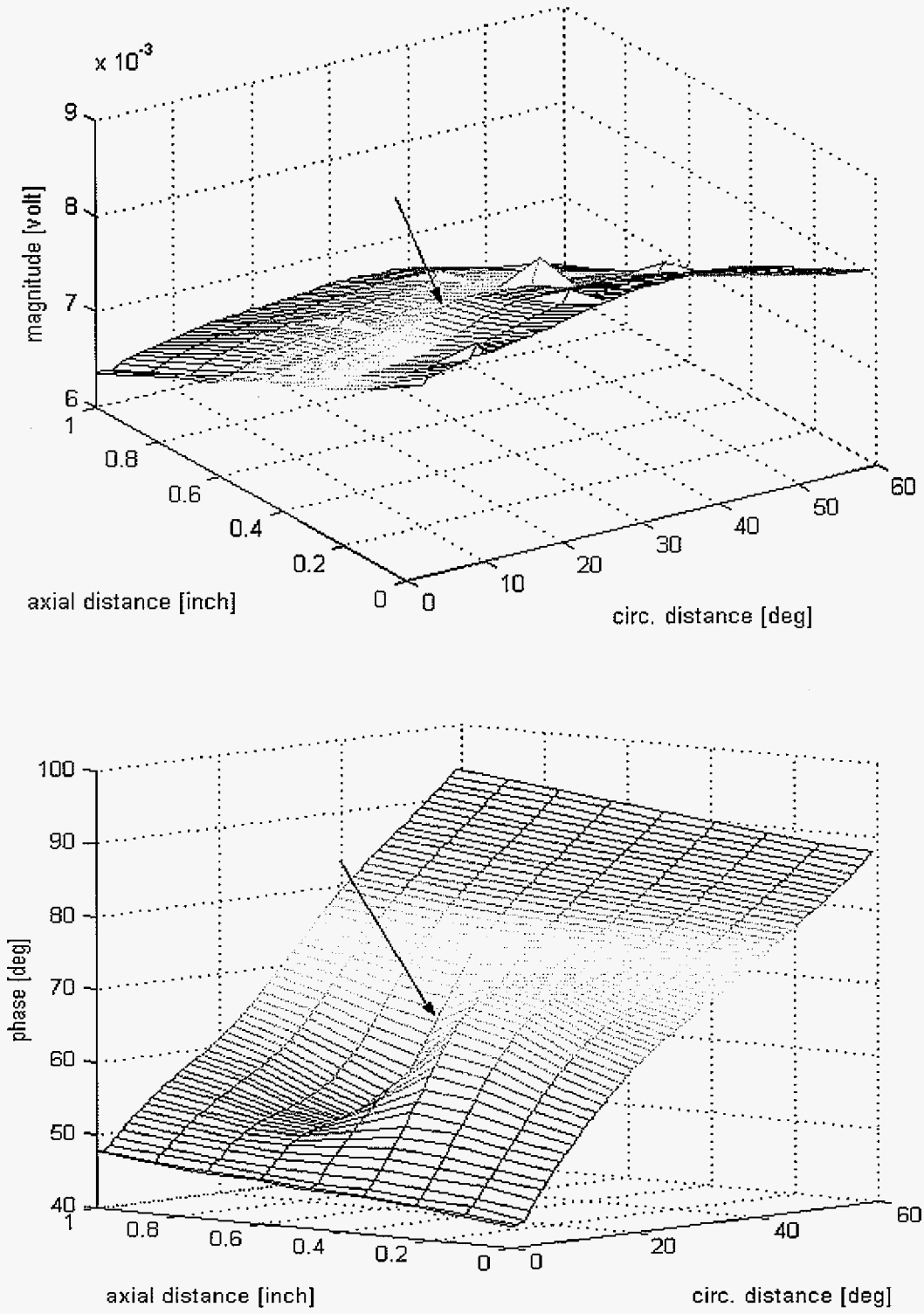

Figure 4.25. 80% deep circumferential notch signals

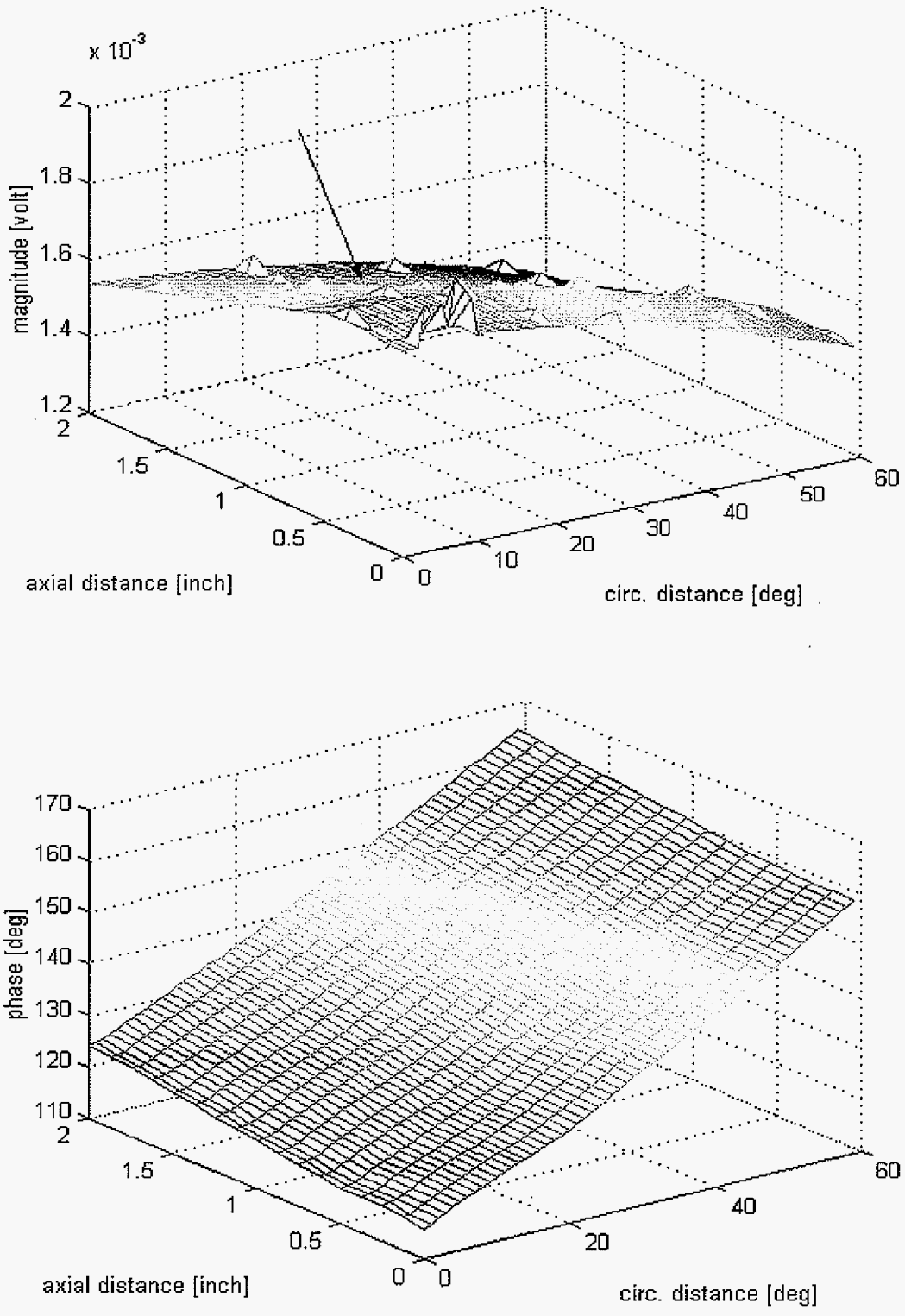

Figure 4.26. 20% deep skewed notch signals

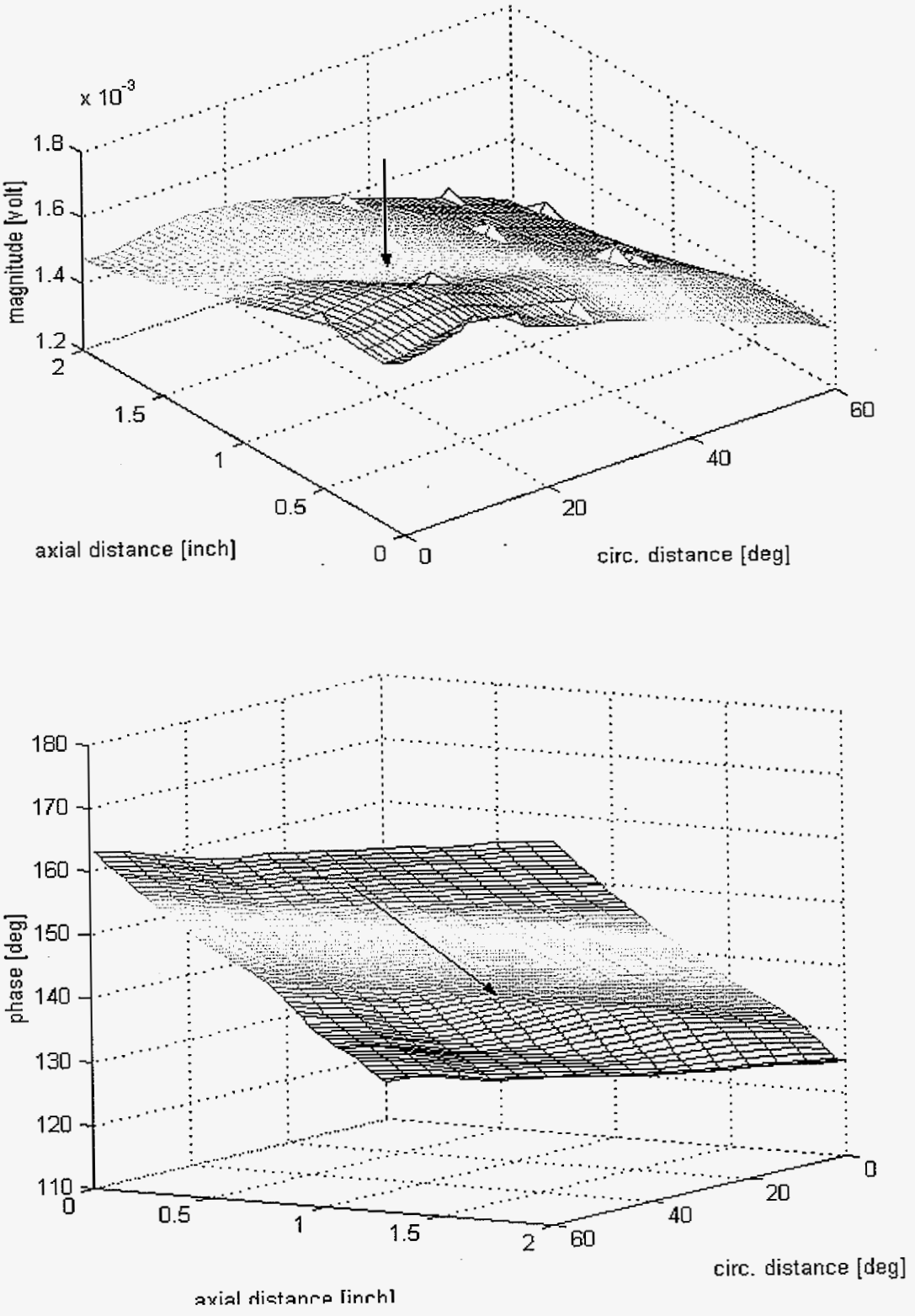

Figure 4.27. 40% deep skewed notch signals

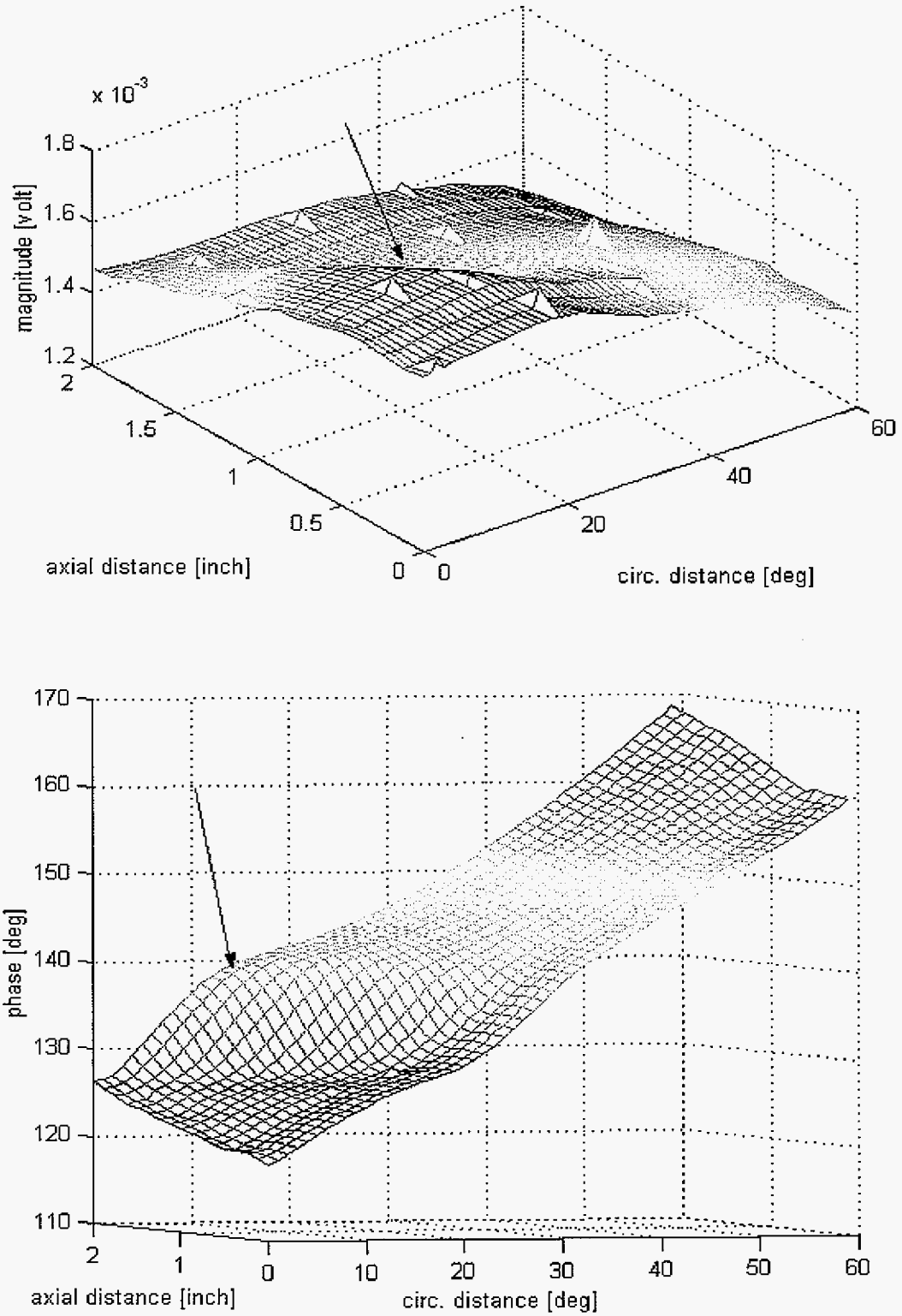

Figure 4.28. 60% deep skewed notch signals

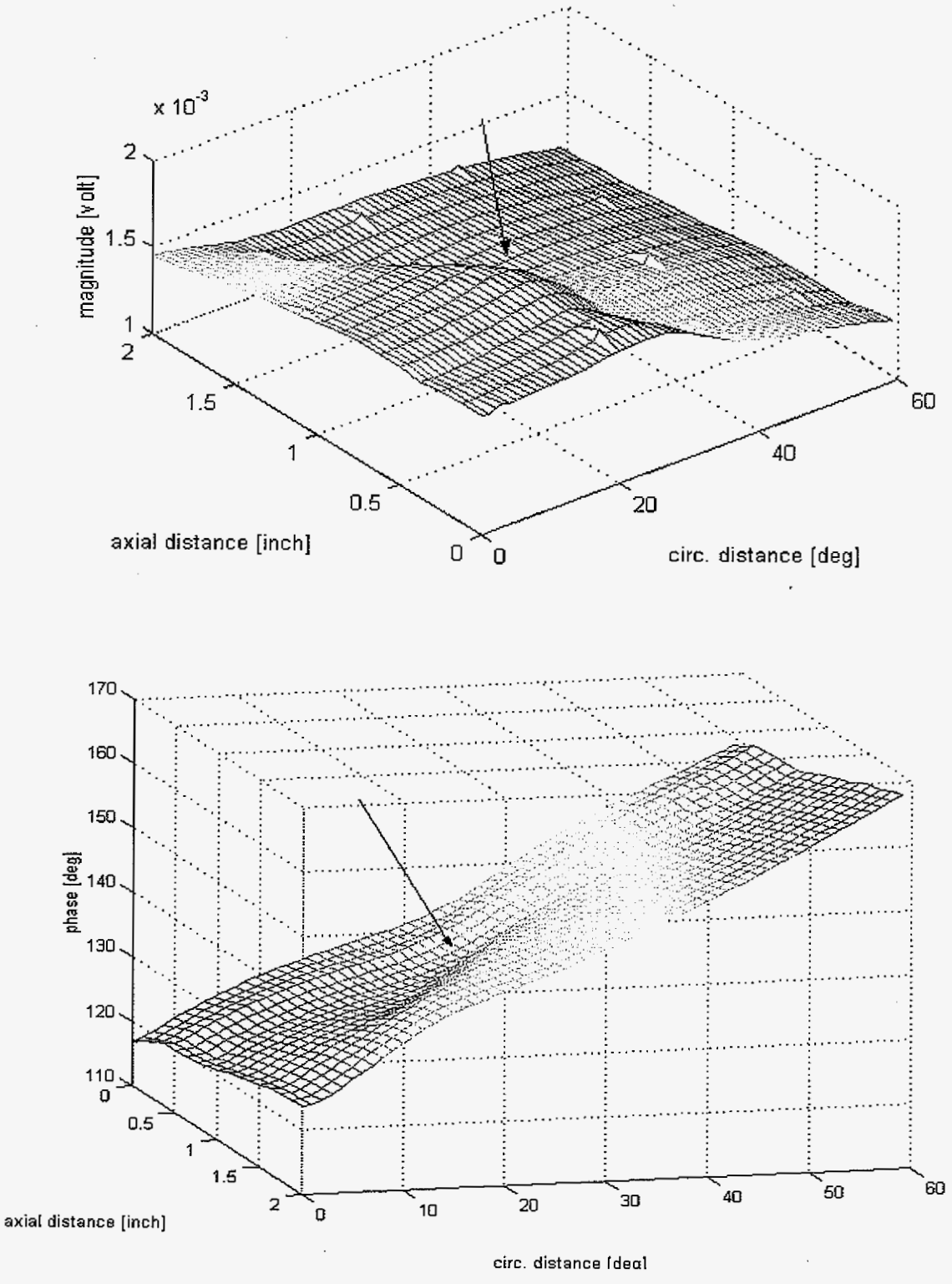

Figure 4.29. 80% deep skewed notch signals

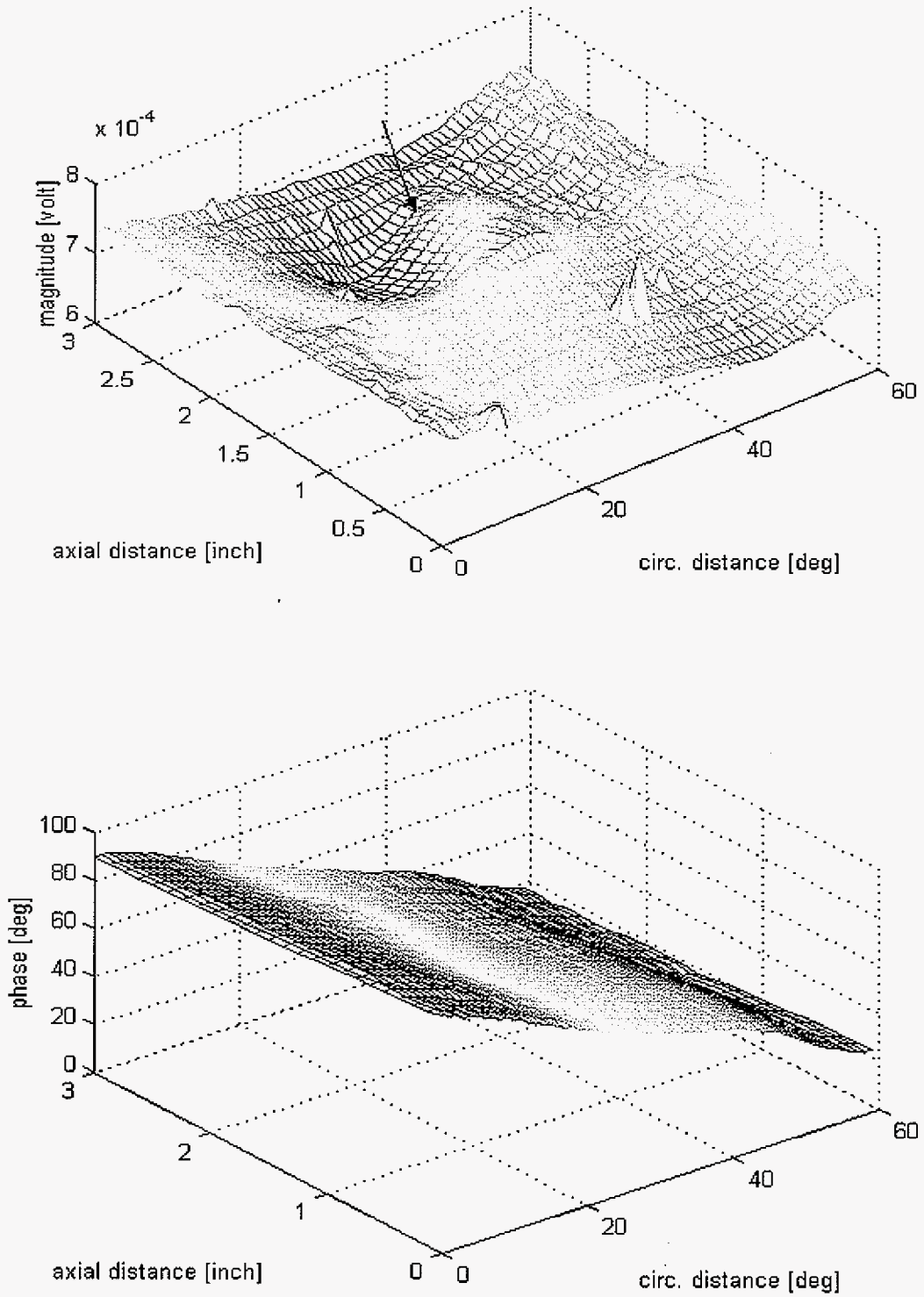

Figure 4.30. 20% deep 1.0" round defect signals

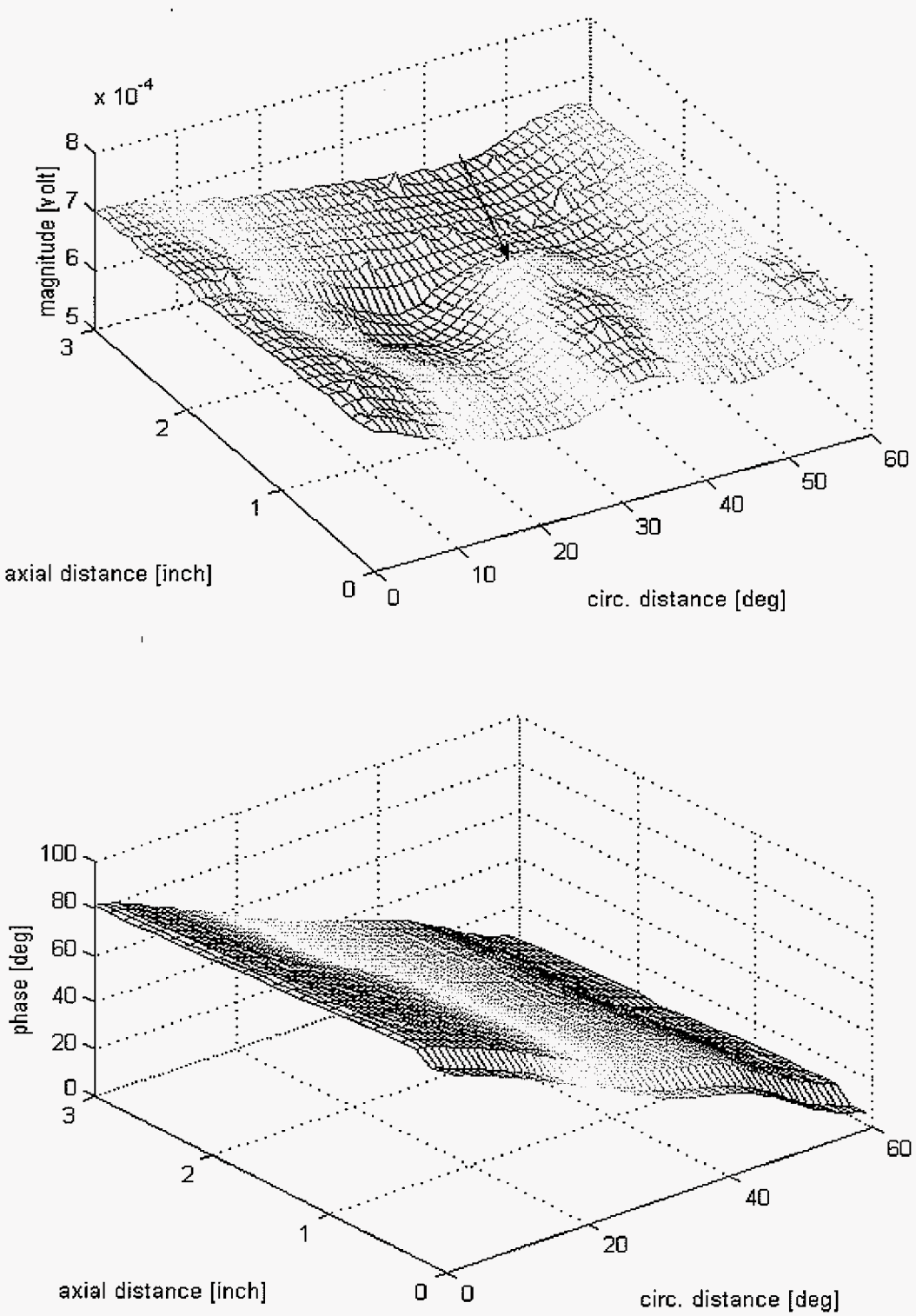

Figure 4.31. 20% deep 1.5" round defect signals

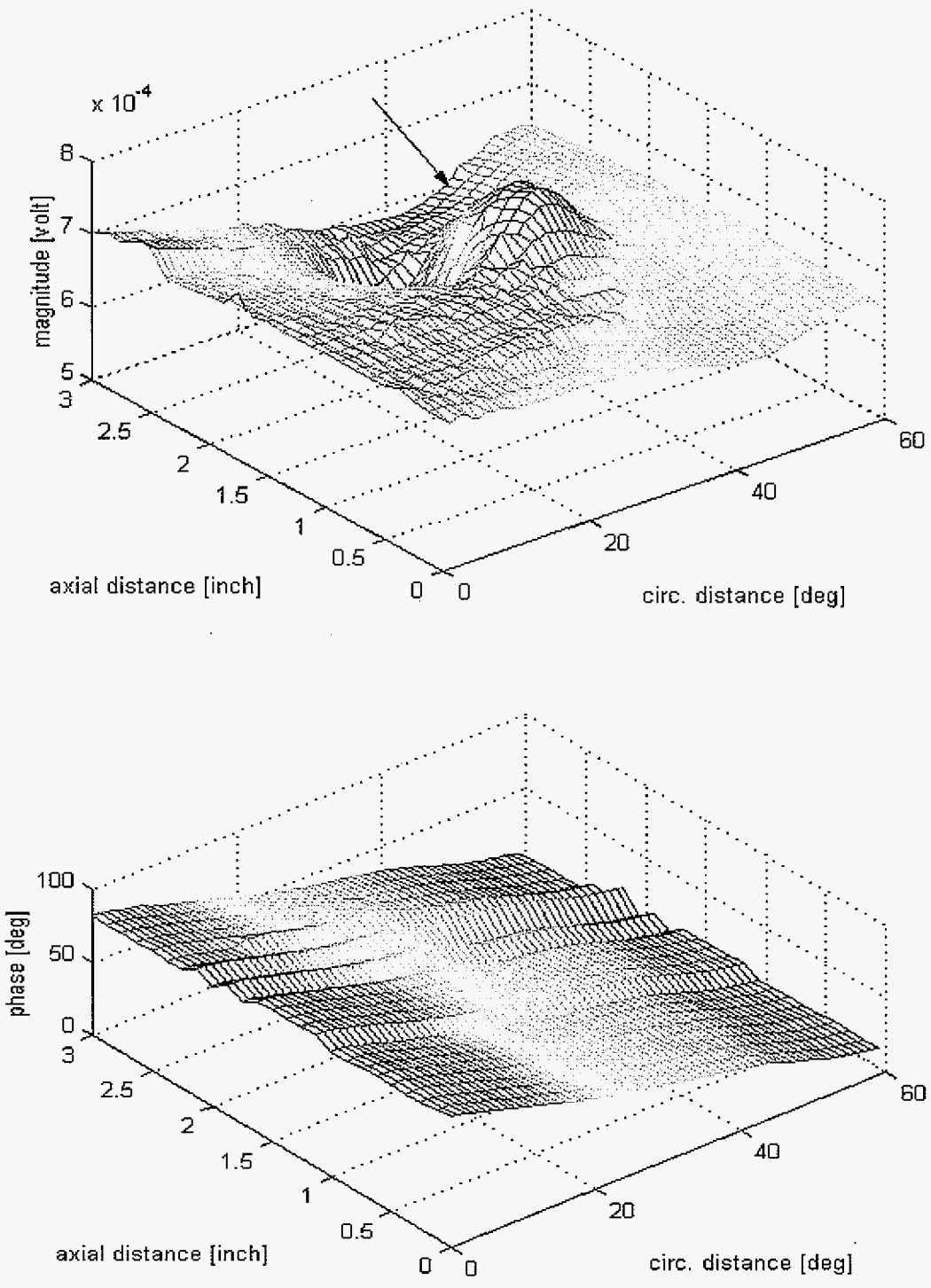

Figure 4.32. 30% deep 1.0" round defect signals

CHAPTER 5. DATA ACQUISITION SYSTEM

5.1. System requirements

This chapter describes the architecture and the development of a data acquisition (DAQ) system designed to enable the detection of SCC. The development of the system presents significant challenges due to its complexity and the required acquisition accuracy, resolution and throughput. The system is designed to operate on an autonomous mobile platform. The platform is propelled through a test pipeline at speeds of up to 10 mph and has to acquire data on the internal surface of the pipeline. The data acquisition has to achieve spatial accuracy of 0.001" and to collect data on 14 channels in real time. An optical shaft angle encoder is used as a "master" clock, because in this application space-based rather than time-based sampling is required. High signal waveform accuracy is required which warrants the use of 16-bit data acquisition device. This is because the useful information is in the signal phase with respect to a measured reference.

The phase measurement requires that at least one full period of the measured sinusoidal signal be registered in order to compare it with the reference sinusoid. In order to minimize measurement errors, the signal has to be averaged over several periods. The static test bed experiments were done using an excitation source with a frequency of 33 Hz. The period of a 33 Hz sinusoidal signal is t=0.030 [s]. The spatial resolution dz required to detect a defect depends on the defect size, sensor size, sensor step and other parameters. The maximum velocity of the inspection tool can then be estimated from the formula: Vmax=dz/t.

As reported in the previous chapter, a resolution of 0.5" was used to detect axially oriented SCC, but a resolution as low as 0.25" was sometimes necessary. A spatial resolution dz=0.25" would limit the velocity of the tool to v=dz/t=8.25 inches per second, which is the same as 825 yards per hour or 0.46 mph. Detecting "small" flaws (SCC, thin cracks) would therefore require inspection speeds as low as 0.5 to 1 mph, "large" flaws, such as a relatively

large diameter (1" or greater) round corrosion pit, would be possible at considerably higher inspection tool velocities.

5.2. Data acquisition boards

Figure 5.1 shows a schematic of the complete DAQ system. The system consists of an array of sensors, located circumferentially on the pipe ID, data acquisition boards, buffer board, PCI board and embedded computer system. The function of the sensors is to register the signal in the remote field. Due to the very low signal levels expected (on the order of 10^{-6} V) a very high gain amplifier is required. The data acquisition boards house a two-cascade amplifier and a serial output A/D device [25]. The function of the PCI board is to interface the outputs of the A/D converters to the data acquisition software on the host PC. Finally, a 133 MHz embedded Penthium system is used as a host, who's only function is to control the PCI board, to store the data stream from the 14 channels and to output it via serial interface or some other way, once a test run is done.

Each sensor is coupled to the input of a two-cascade amplifier. The first cascade is a differential input pre-amplifier with a gain of 40 dB [26] built on a chopper-stabilized low noise operating amplifier LT1050 [27]. The use of a chopper-stabilized amplifier is necessary due to the low operating frequency of the system. Static test bed experiments indicated that the optimal frequency of the excitation source is around 33 Hz. At such low frequencies the so-called 1/f noise becomes significant. Chopper-stabilized amplifiers are designed to minimize the 1/f noise and are therefore extremely useful in low-frequency applications.

The second cascade of the analog front-end is built on an LT1069 gain programmable operating amplifier [28]. This device is capable of producing a gain of up to 100 dB. The gain of the second cascade is selected by changing the gain resistor on the device. Four gain selections are possible.

Due to the large gain in the first cascade direct coupling to the second cascade would not be possible because of the DC component of the output. The first and the second cascades are coupled using a band-pass filter. The band-pass filter used is a passive classical

four-element network [29]. The filter is tuned at a center frequency of 33 Hz. This network is very inefficient, but it was chosen due to space constraints on the printed circuit board. The same is true for the first cascade – the simplest possible amplifier configuration was adopted.

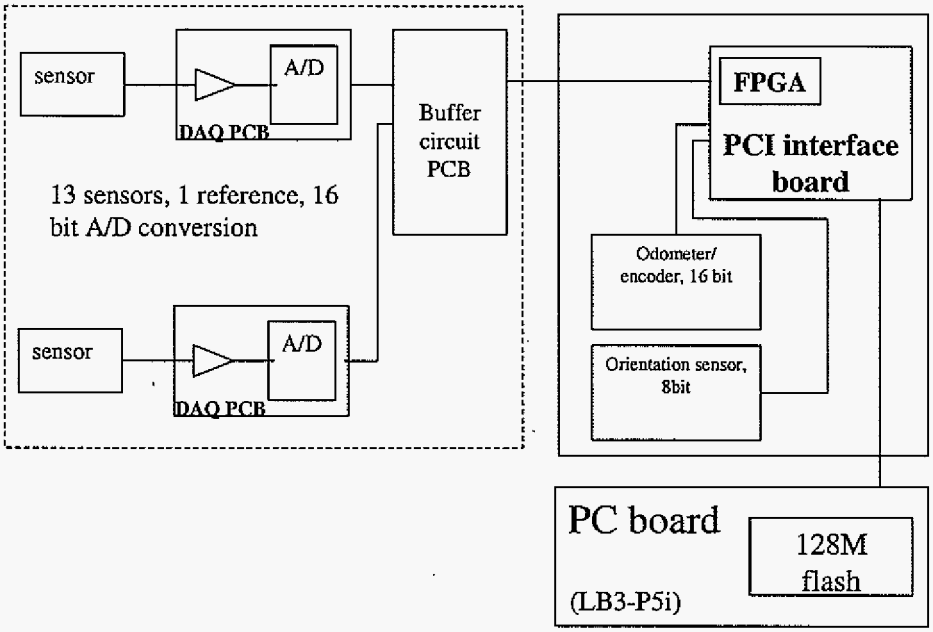

Figure 5.1. Milti-channel real-time data acquisition system

5.3. PCI board architecture

Figure 5.2 shows a schematic of the PCI board architecture. The PCI board houses the following main elements:

- 40 connector to DAQ assembly;
- FPGA with configuration chip;
- 2 dual port 64K memory arrays;
- PCI controller with configuration chip
- PCI bus connector to the host computer

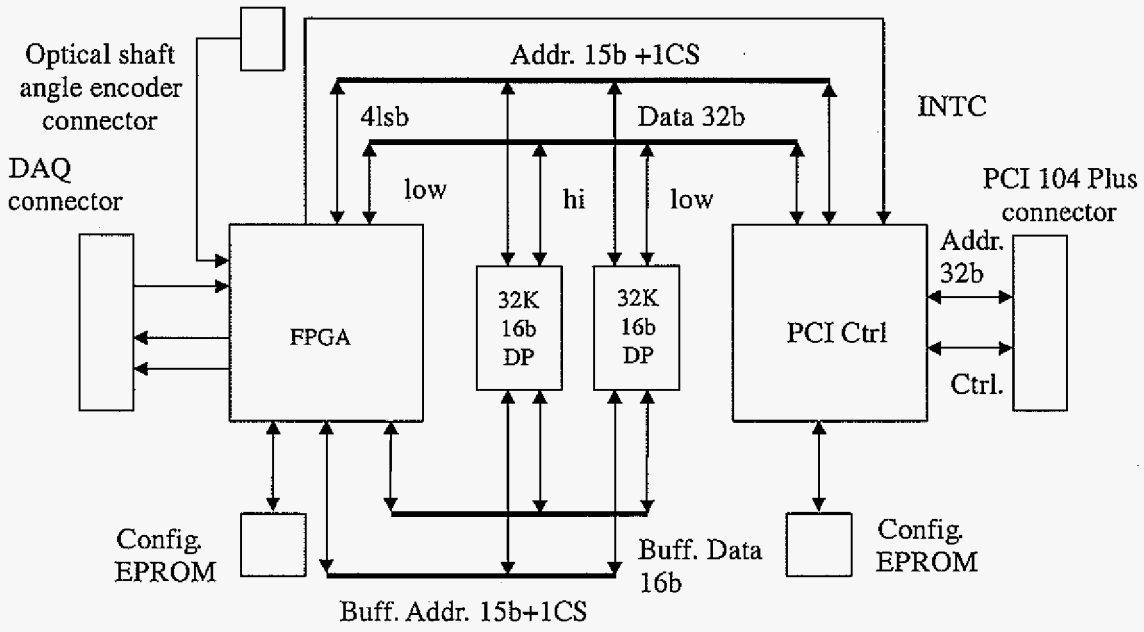

Figure 5.2. Interface board architecture

The FPGA is the heart of the data acquisition system. The FPGA has to be configured to communicate with the 14 A/D converters, the buffer memory and the host PC. The FPGA has to sense the signal from the optical shaft angle encoder, calculate the tool velocity and trigger the acquisition, produce clocking and control signals for the A/D converters, then generate addresses and store in the memory buffer the content of 16, 16-bit registers. The FPGA should also monitor the availability of buffer memory space and inform the PC that data is available for transfer to the PC RAM disk. Additionally the FPGA would compute a cyclic redundancy check code for the 14 data values and 1 velocity value stored in the registers.

The function of the on-board memory is to provide sufficient buffer space. The FPGA can be configured such that after half of the buffer is filled it would generate an interrupt. The interrupt will prompt the host computer to read the buffer, while the FPGA continues to fill the remaining space in the buffer. The host computer will always be able to read the data

from the buffer before any new data comes in the first half of the buffer. This type of memory can be read from and written to at the same time.

The FPGA and the PCI controller access the memory bank on separate busses. The function of the PCI controller is to provide the signaling necessary for communication with the host computer. The PCI controller maps the buffer address space into the host computer's address space. The host computer can also address registers inside the FPGA. This may be necessary for synchronization purposes.

5.4. FPGA configuration

The most essential element of the system is the configuration of the FPGA. Figure 5.3 shows a schematic of the FPGA configuration.

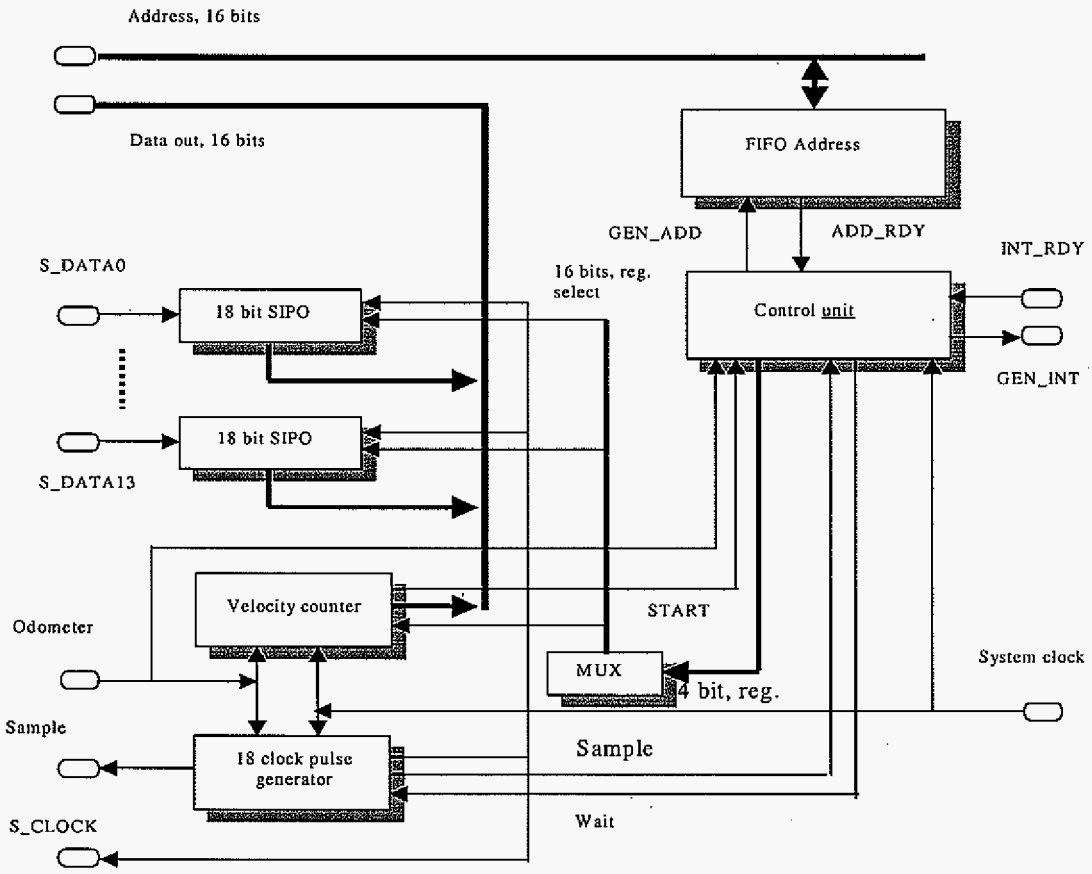

Figure 5.3. FPGA configuration

The configuration includes 14 18 bit serial in, parallel out (SIPO) shift registers, data bus, address bus, multiplexer, 18 pulses clock generator, velocity circuit, FIFO address generator and a control circuit. The data value from each of the 14 A/D converters has to be obtained at the same time. The AD977A is a serial output device and the function of the SIPO registers is to store the data value from the converter. There is a slight complication in the process arising from the fact, that the last bit value out of AD977A is available between the falling edge of the 16^{th} clock cycle and rising edge of the 17^{th} clock cycle [25]. Therefore a minimum of 17 cycles is needed to read a data sample the 18^{th} cycle is there to "flush" the output buffer of the device and prevent errors.

The function of the 18 pulses clock generator is to generate the clocking signal necessary to read the data sample in a serial fashion from the A/D converters. The pulse generation is triggered by the rising edge of the odometer wheel signal. The odometer wheel is used as a "master" clock. Each rising edge triggers the acquisition of 15 data values plus one cyclic redundancy check code computed from the data, which have to be put on the data bus and transferred via the PCI to the memory of the embedded computer, before the next edge arrives. Selection of the pulse clock generator frequency would require some experimentation.

The function of the velocity circuit is to measure the velocity of the tool. The velocity is measured by counting the number of system clock cycles occurring between wheel impulses. A velocity value is put on the data bus for each wheel impulse. This may prove to be a significant and unnecessary overhead and may need to be re-configured in the future.

The function of the control block is to organize the data flow from the registers to the memory of the embedded computer system. The control circuit together with the multiplexer selects, which of the data values is put on the bus. It also generates an interrupt to the PCI controller, the control signal to the A/D converters and the FIFO address generation structure. The FIFO address circuit is responsible for maintaining a buffer in the temporary memory on the interface board.

Figure 5.4 shows the schematic of the address generation circuit and figure 5.5 shows the simulation of the circuit. The address generator is realized as a 16 bit counter, which

increases its output value on the falling edge of the signal "next" fed to the clock of the counter. The counter has an asynchronous clear input (which can be used to reset the counter value to h0000). Fig.5 illustrates the simulation results. The output value of "buff_addr" is increased for each falling edge of "next".

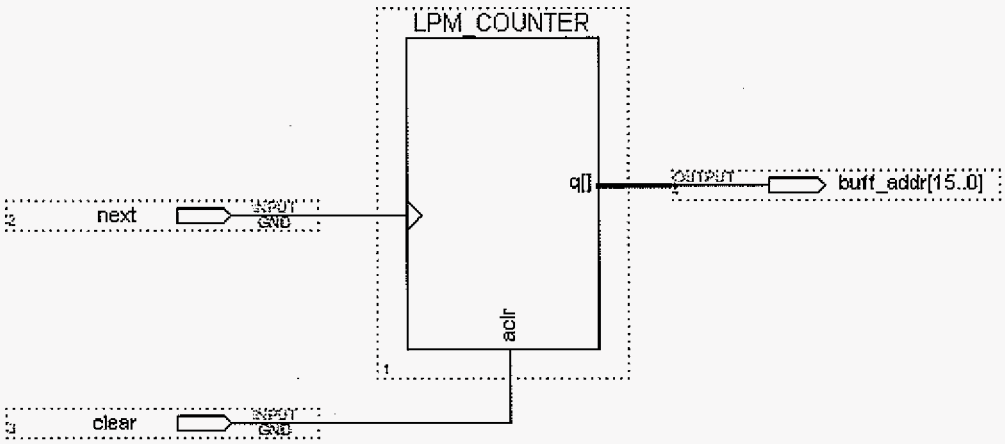

Figure 5.4. Address generator

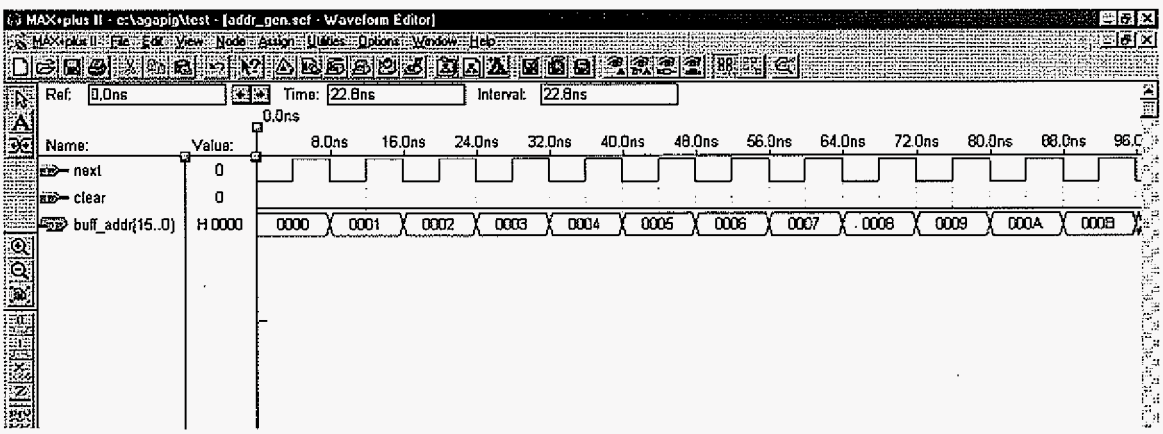

Figure 5.5. Address generator simulation

The clock generator, a schematic of which is shown on figure 5.6. senses the rising edge of the optical shaft angle encoder to start the clock generation. It clears a counter, whose value is subsequently increased at each clock pulse and compared to a limiting constant – 18. Once 18 pulses are generated on the "s_clock" output, the counter remains disabled until a new pulse from the shaft angle encoder is sensed. During counting output signals "busy" and "r_c" are set low and high respectively.

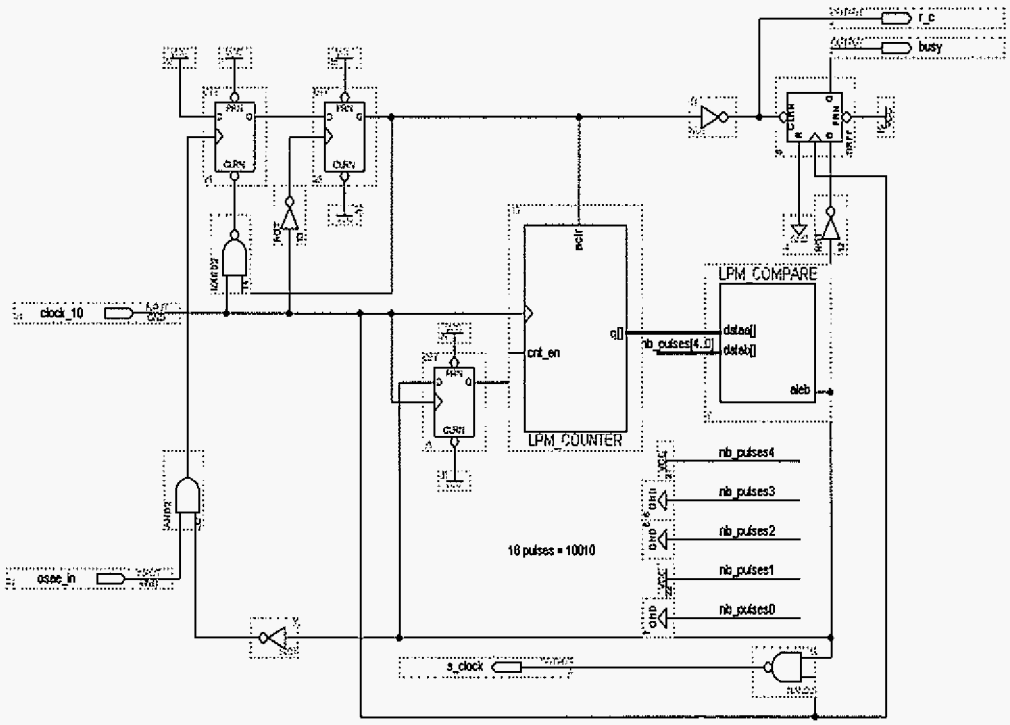

Figure 5.6. Clock generator

Figure 5.7 below shows the simulation of the clock generator. The most important problem, which the generating circuit would have is jitter on the shaft angle encoder signal. The circuit is designed so that it would not restart the counting if a shaft angle encoder pulse arrives before the 18 "s_clock" pulses were generated. Note on figure 5.7 that, the rising edge of the "osae_in" arriving just after 0.0us triggers the clock generation, but the rising edge arriving just before 1.0us does not.

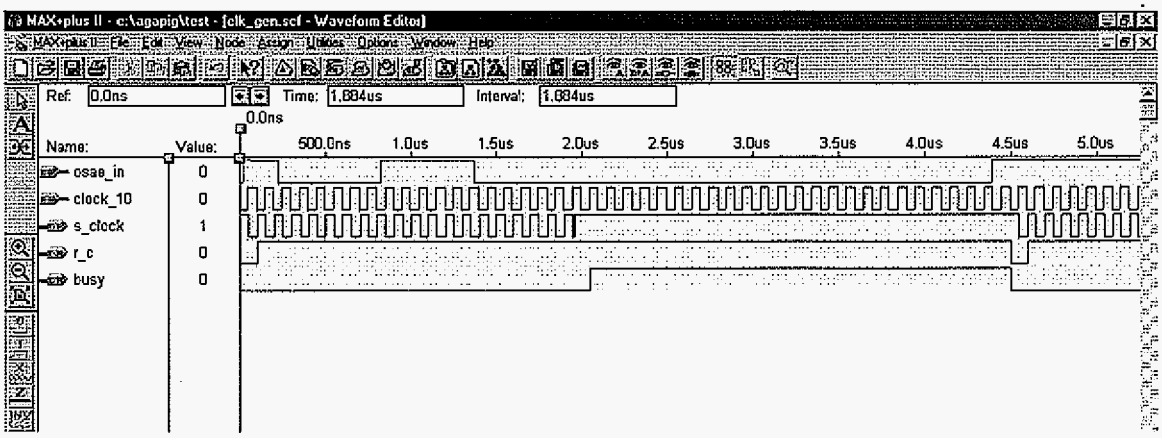

Figure 5.7. Clock generator simulation

The control block is realized as a state machine. A description of the state machine in VHDL follows.

```
SUBDESIGN control
(
clock, sample, start                          :INPUT;
crc_add, gen_addr, enable_clk, reg_sel[3..0] :OUTPUT;
)
VARIABLE
        ctrl : MACHINE WITH STATES (
                        wait,
                        enable,
                        reg0_0, reg0_1, reg0_2, reg0_3,
                        reg1_0,     reg1_1,     reg1_2,     reg1_3,
                        reg2_0,     reg2_1,     reg2_2,     reg2_3,
                        reg3_0,     reg3_1,     reg3_2,     reg3_3,
                        reg4_0,     reg4_1,     reg4_2,     reg4_3,
```

```
                    reg5_0,     reg5_1,     reg5_2,     reg5_3,
                    reg6_0,     reg6_1,     reg6_2,     reg6_3,
                    reg7_0,     reg7_1,     reg7_2,     reg7_3,
                    reg8_0,     reg8_1,     reg8_2,     reg8_3,
                    reg9_0,     reg9_1,     reg9_2,     reg9_3,
                    reg10_0,    reg10_1,    reg10_2,    reg10_3,
                    reg11_0,    reg11_1,    reg11_2,    reg11_3,
                    reg12_0,    reg12_1,    reg12_2,    reg12_3,
                    reg13_0,    reg13_1,    reg13_2,    reg13_3,
                    reg14_0,    reg14_1,    reg14_2,    reg14_3,
                    reg15_0,    reg15_1,    reg15_2,    reg15_3 );
BEGIN
        ctrl.clk = clock;
        TABLE
        % Present state        Inputs  => Next state  Outups %
        ctrl,   start,  sample =>ctrl, enable_clk,    crc_add,      gen_addr,
        reg_sel[3..0];
        wait,   0,      X       =>      wait,   0,      0,      0,      0;
        wait,   1,      X       =>      enable, 1,      0,      0,      0;
        enable, 0,      X       =>      wait,   0,      0,      0,      0;
        enable, 1,      1       =>      reg0_0,         1,      0,      0,      0;
        reg0_0,         X,      X       =>      reg0_1,         1,      0,      1,      0;
        reg0_1,         X,      X       =>      reg0_2,         1,      0,      0,      0;
        reg0_2,         X,      X       =>      reg0_3,         1,      1,      0,      0;
        reg0_3,         X,      X       =>      reg1_0,         1,      0,      0,      0;
        reg1_0,         X,      X       =>      reg1_1,         1,      0,      1,      1;
        reg1_1,         X,      X       =>      reg1_2,         1,      0,      0,      1;
        reg1_2,         X,      X       =>      reg1_3,         1,      1,      0,      1;
        reg1_3,         X,      X       =>      reg2_0,         1,      0,      0,      1;
        reg2_0,         X,      X       =>      reg2_1,         1,      0,      1,      2;
```

```
reg2_1,    X,    X    =>    reg2_2,    1,    0,    0,    2;
reg2_2,    X,    X    =>    reg2_3,    1,    1,    0,    2;
reg2_3,    X,    X    =>    reg3_0,    1,    0,    0,    2;
reg3_0,    X,    X    =>    reg3_1,    1,    0,    1,    3;
reg3_1,    X,    X    =>    reg3_2,    1,    0,    0,    3;
reg3_2,    X,    X    =>    reg3_3,    1,    1,    0,    3;
reg3_3,    X,    X    =>    reg4_0,    1,    0,    0,    3;
reg4_0,    X,    X    =>    reg4_1,    1,    0,    1,    4;
reg4_1,    X,    X    =>    reg4_2,    1,    0,    0,    4;
reg4_2,    X,    X    =>    reg4_3,    1,    1,    0,    4;
reg4_3,    X,    X    =>    reg5_0,    1,    0,    0,    4;
reg5_0,    X,    X    =>    reg5_1,    1,    0,    1,    5;
reg5_1,    X,    X    =>    reg5_2,    1,    0,    0,    5;
reg5_2,    X,    X    =>    reg5_3,    1,    1,    0,    5;
reg5_3,    X,    X    =>    reg6_0,    1,    0,    0,    5;
reg6_0,    X,    X    =>    reg6_1,    1,    0,    1,    6;
reg6_1,    X,    X    =>    reg6_2,    1,    0,    0,    6;
reg6_2,    X,    X    =>    reg6_3,    1,    1,    0,    6;
reg6_3,    X,    X    =>    reg7_0,    1,    0,    0,    6;
reg7_0,    X,    X    =>    reg7_1,    1,    0,    1,    7;
reg7_1,    X,    X    =>    reg7_2,    1,    0,    0,    7;
reg7_2,    X,    X    =>    reg7_3,    1,    1,    0,    7;
reg7_3,    X,    X    =>    reg8_0,    1,    0,    0,    7;
reg8_0,    X,    X    =>    reg8_1,    1,    0,    1,    8;
reg8_1,    X,    X    =>    reg8_2,    1,    0,    0,    8;
reg8_2,    X,    X    =>    reg8_3,    1,    1,    0,    8;
reg8_3,    X,    X    =>    reg9_0,    1,    0,    0,    8;
reg9_0,    X,    X    =>    reg9_1,    1,    0,    1,    9;
reg9_1,    X,    X    =>    reg9_2,    1,    0,    0,    9;
reg9_2,    X,    X    =>    reg9_3,    1,    1,    0,    9;
```

```
        reg9_3,     X,   X   =>  reg10_0,    1,   0,   0,   9;
        reg10_0,    X,   X   =>  reg10_1,    1,   0,   1,   10;
        reg10_1,    X,   X   =>  reg10_2,    1,   0,   0,   10;
        reg10_2,    X,   X   =>  reg10_3,    1,   1,   0,   10;
        reg10_3,    X,   X   =>  reg11_0,    1,   0,   0,   10;
        reg11_0,    X,   X   =>  reg11_1,    1,   0,   1,   11;
        reg11_1,    X,   X   =>  reg11_2,    1,   0,   0,   11;
        reg11_2,    X,   X   =>  reg11_3,    1,   1,   0,   11;
        reg11_3,    X,   X   =>  reg12_0,    1,   0,   0,   11;
        reg12_0,    X,   X   =>  reg12_1,    1,   0,   1,   12;
        reg12_1,    X,   X   =>  reg12_2,    1,   0,   0,   12;
        reg12_2,    X,   X   =>  reg12_3,    1,   1,   0,   12;
        reg12_3,    X,   X   =>  reg13_0,    1,   0,   0,   12;
        reg13_0,    X,   X   =>  reg13_1,    1,   0,   1,   13;
        reg13_1,    X,   X   =>  reg13_2,    1,   0,   0,   13;
        reg13_2,    X,   X   =>  reg13_3,    1,   1,   0,   13;
        reg13_3,    X,   X   =>  reg14_0,    1,   0,   0,   13;
        reg14_0,    X,   X   =>  reg14_1,    1,   0,   1,   14;
        reg14_1,    X,   X   =>  reg14_2,    1,   0,   0,   14;
        reg14_2,    X,   X   =>  reg14_3,    1,   1,   0,   14;
        reg14_3,    X,   X   =>  reg15_0,    1,   0,   0,   14;
        reg15_0,    X,   X   =>  reg15_1,    1,   0,   1,   15;
        reg15_1,    X,   X   =>  reg15_2,    1,   0,   0,   15;
        reg15_2,    X,   X   =>  reg15_3,    1,   1,   0,   15;
        reg15_3,    X,   X   =>  enable,     1,   0,   0,   15;
        END TABLE;
END;
```

Figure 5.8 shows the operation of the control block state machine, once a signal "start" sets high (i.e. acquisition, should begin), the "enable_clk" output is set high, to enable

the clock generation circuit. The rising edge of the "sample" signal starts the state machine. The "reg_select" output is set to a value from 0 to F, which allows each of the 16 registers to put data on the data bus. The signals "gen_addr" and "crc_add" cause an address to be generated on the address bus and the value of the data bus to be accumulated in the CRC register.

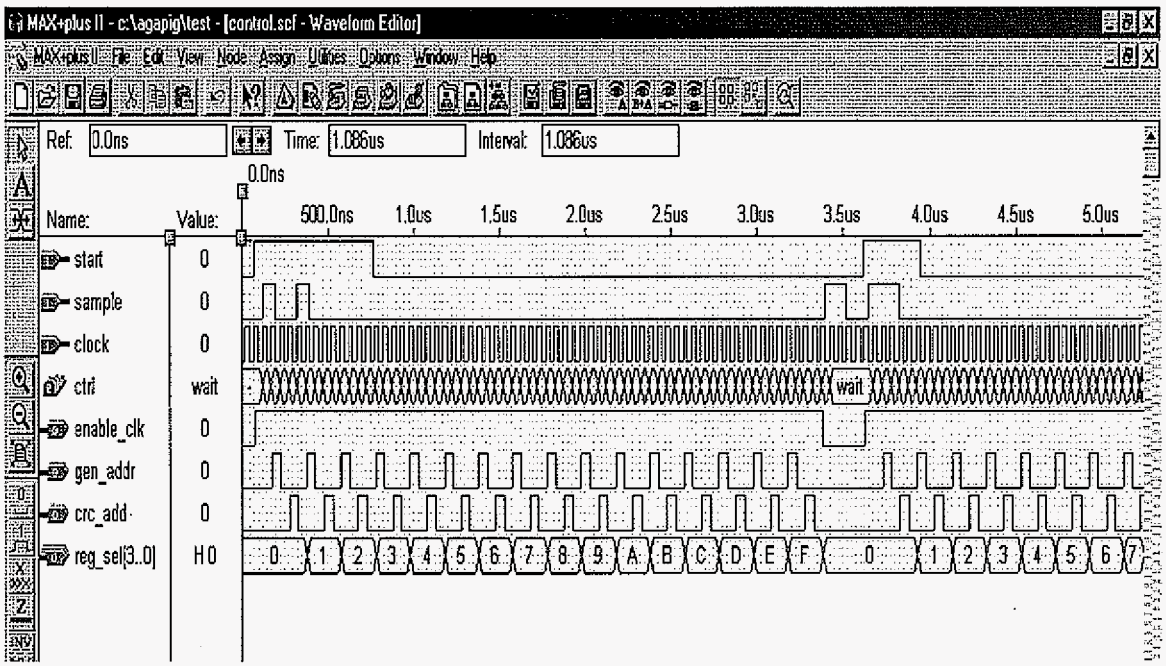

Figure 5.8. Control block simulation

Figure 5.9. shows the schematic of the CRC block. It is realized as a set of 16 XOR gates, which adds the value on the data bus to the one previously stored in the register (a set of D flip-flops). The accumulation is done at the rising edge of the "add" signal. The circuit also has a tri-state buffered output, i.e. the outputs of the CRC register are in high impedance state, until "enable" signal is set to high.

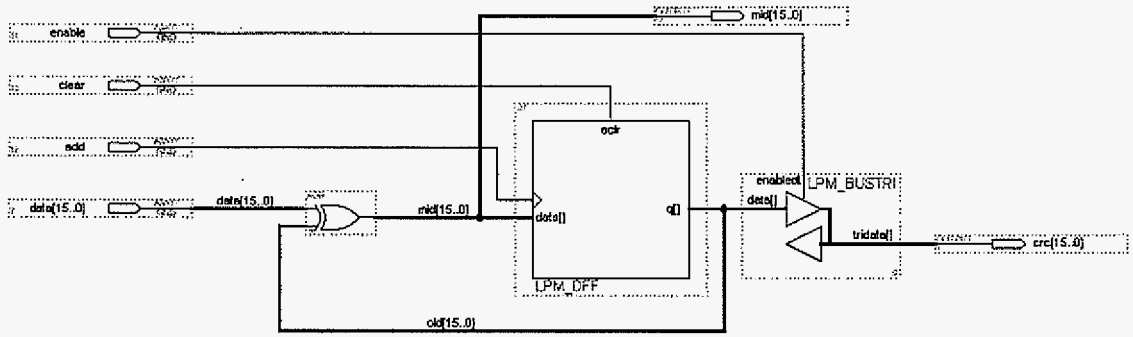

Figure 5.9. CRC block

Figure 5.10. shows a simulation of the CRC register. The values of h0000, hF0F0, h0F0F, hFFFF are accumulated in the CRC register, which sets the output to h0000, hF0F0, hFFFF, h0000 at each rising edge of the "add" signal, while "enable" is set to high. A high on "clear" resets the output to h0000.

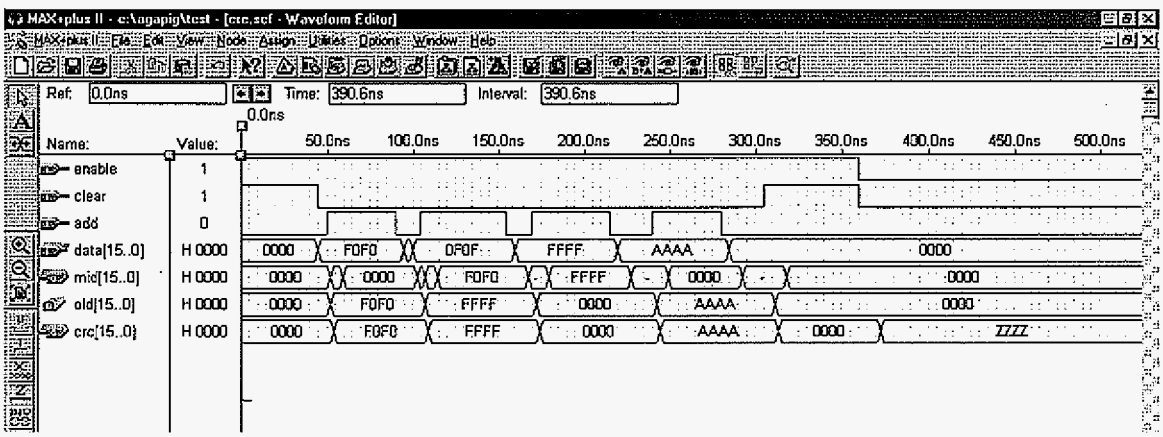

Figure 5.10. CRC block simulation

The register address circuit is realized by a 16-bit decoder, which is shown on figure 5.11. The decoding is done on the rising edge of the clock and sets only one of the 16

"reg_sel" outputs to high, which enables the tri-state output of the appropriate register and allows the data contained in it on the data bus.

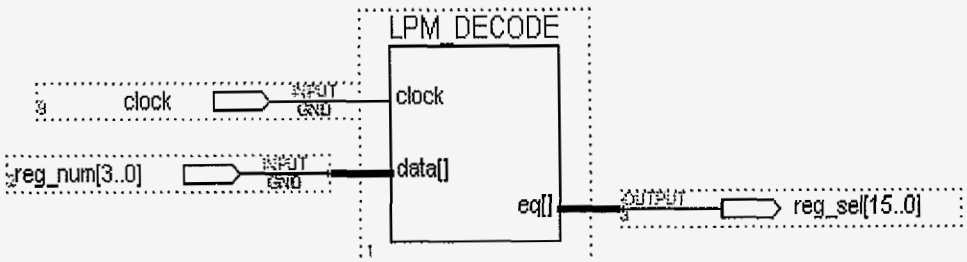

Figure 5.11. Register address circuit

Figure 5.12 shows the simulation of the register address circuit. The value of "reg_num" is increased from 0 to F and the decoder correctly activates the outputs "reg_sel0" through "reg_sel15".

The function of the INT generator is to generate an interrupt every time one of the memory banks fills up, i.e. every time addresses h8000 and hFFFF show on the address bus. The interrupt informs the computer to read the entire bank of data, while the next one is being filled with data. Thus the data rate is limited by the speed with which the host processor can read the data flow over the PCI bus. The INT generator is realized as a sum of the outputs of two comparators, one comparing the address (on the "data" input) to h8000 and the other to hFFFF.

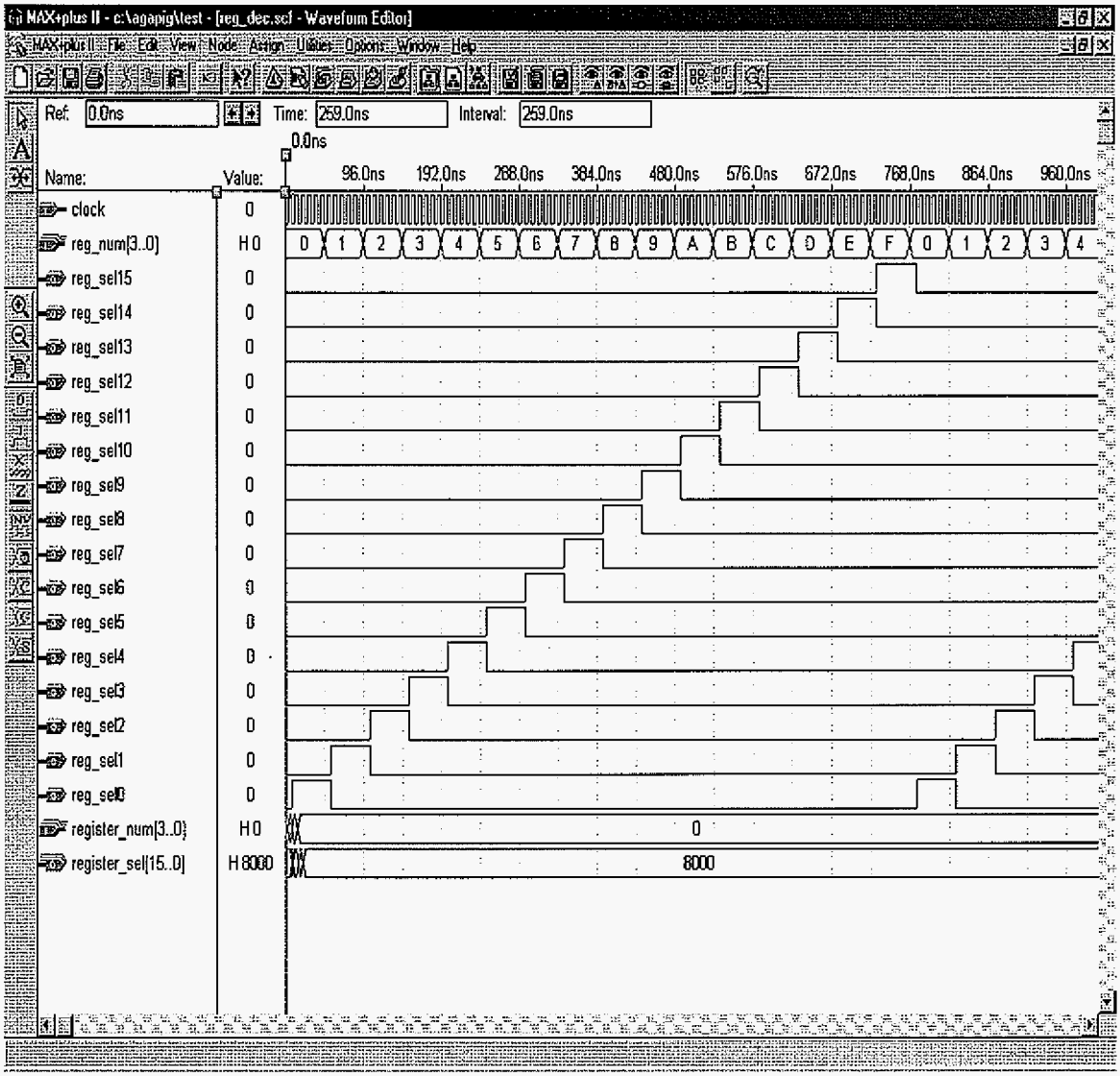

Figure 5.12. Register address circuit simulation

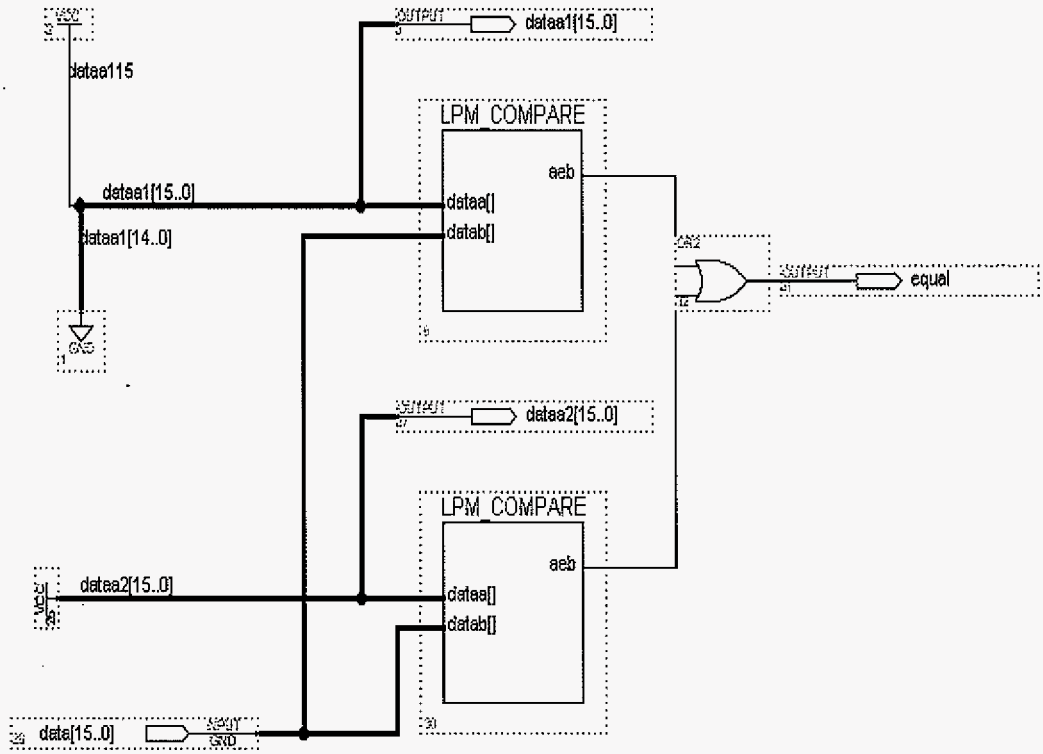

Figure 5.13. INT generator

Figure 5.14 shows a simulation of the INT generator. Note, that the output "equal" sets to high every time h8000 or hFFFF shows on the "data" input. There is a delay of at least 8 ns for the comparators to settle, but this delay is insignificant. The INT signal stays high until the next data sample is acquired.

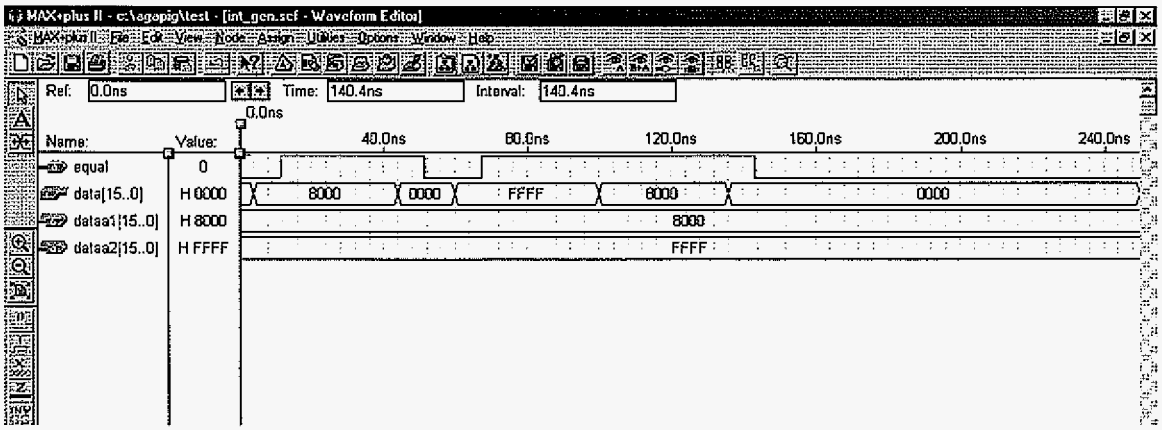

Figure 5.14. INT generator simulation

The SIPO circuit is realized by an 18 bit shift register, whose 16 most significant bits are connected to a tri-state buffering circuit. As already stated the AD977A requires at lest 17 clock cycles to output a data sample, therefore two of the bits are dropped. The outputs of the register are in high impedance state, until the "enable" signal is set to high.

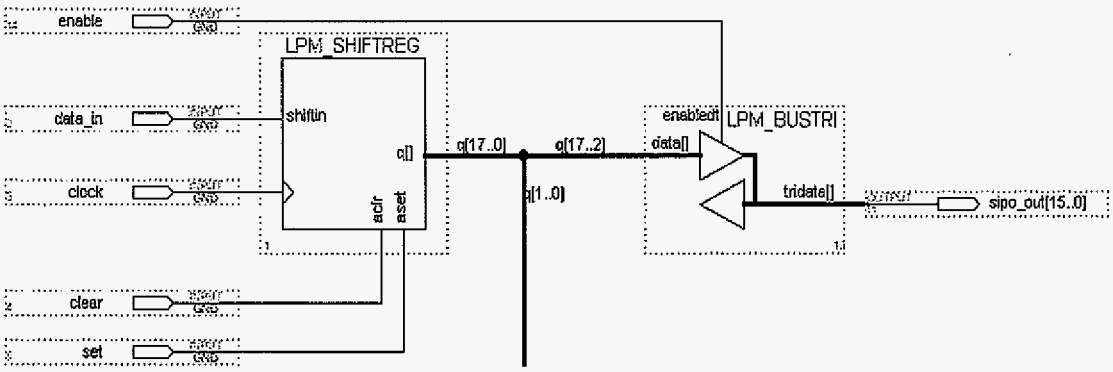

Figure 5.15. SIPO schematic

Figure 5.16 shows a simulation of the SIPO circuit. The data on "data_in" line is shifted in the register, while the outputs are in high impedance state. When the "enable" signal is set to high the correct value b1101101000111100 is output on "sipo_out0" thorough "sipo_out15". A high on "clear" clears the outputs to zero. Note that the value of "data_in" is sensed on the rising edge of the clock.

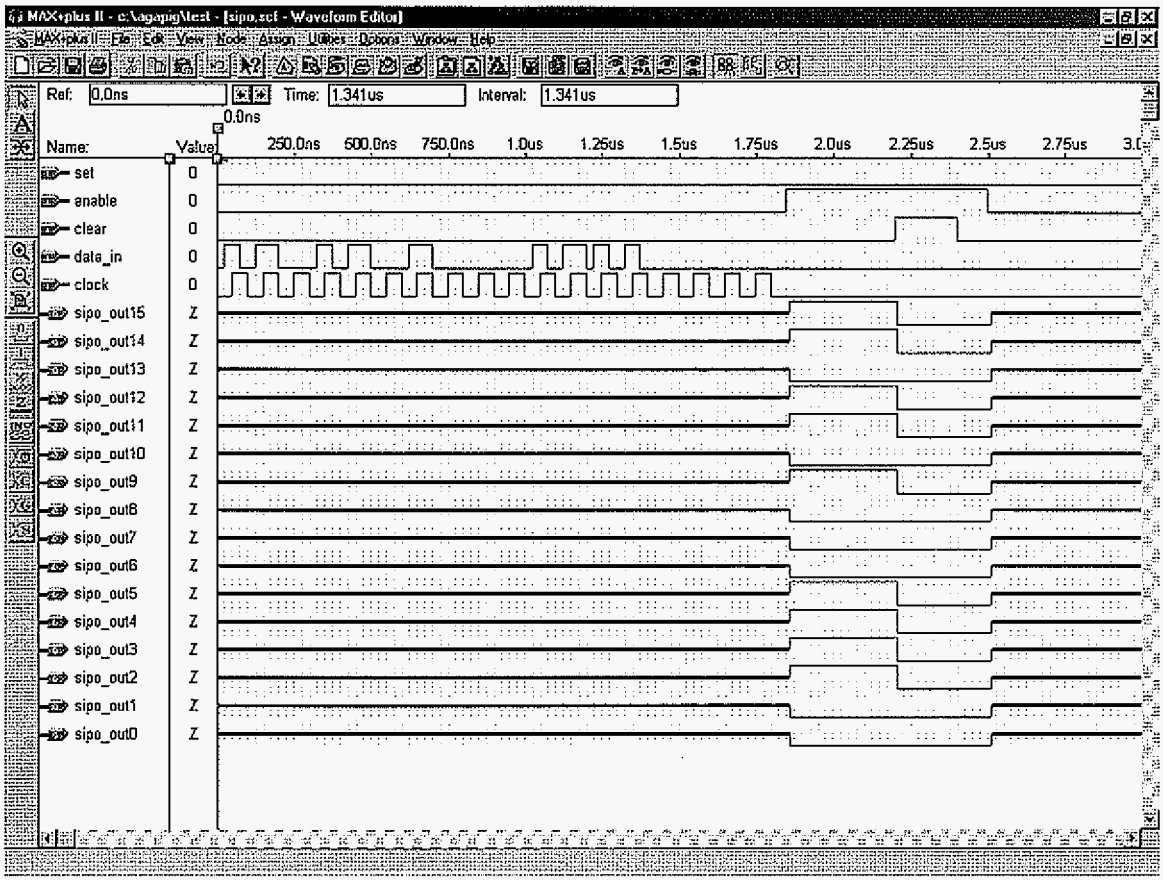

Figure 5.16. SIPO simulation

The velocity counter circuit (shown of figure 5.17) senses the output of the optical shaft angle encoder and counts the number of clock cycles between two consecutive "osae_in" pulses. The counter value is stored into a set of D flip-flops and is output when the "enable" signal is set to high. As with all the other registers the outputs are tri-state buffered. A comparator is used to determine when the acquisition should begin (i.e. at what velocity).

This is necessary, since even with the tool motionless, the shaft angle encoder will produce "noise" pulses occasionally and those should not trigger a sample acquisition.

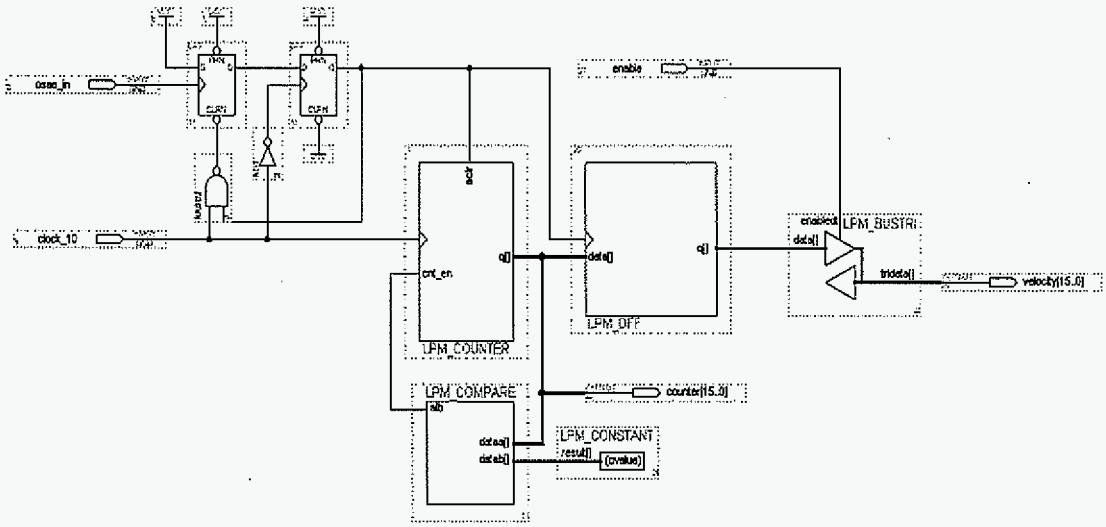

Figure 5.17. Velocity counter

Figure 5.18 shows the simulation results obtained from the velocity counter circuit. Note, that when the "enable" signal is set to high, the last value stored in the flip-flops is h50F2. This value is obtained from "osae_in" pulses, that are not visible in the window.

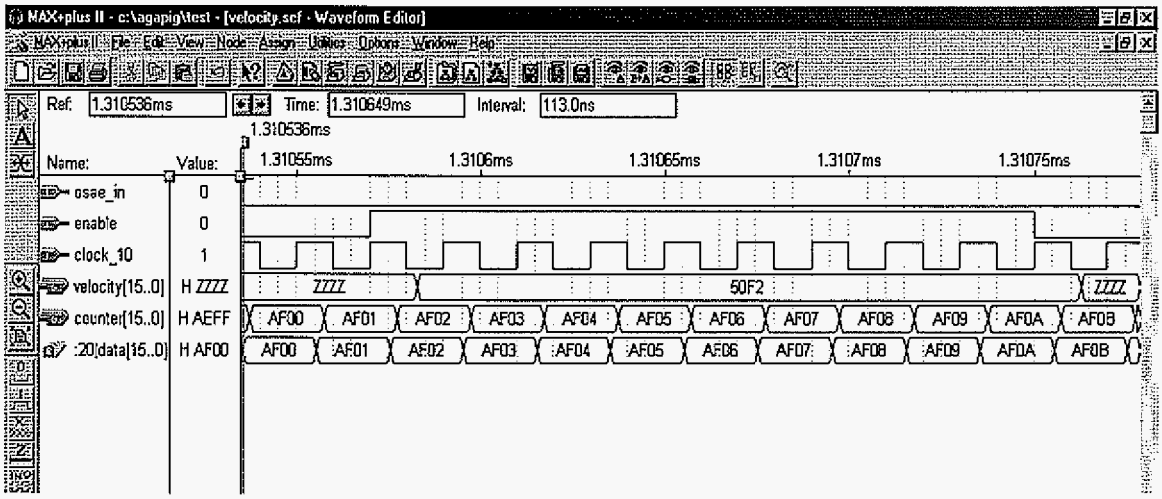

Figure 5.18. Velocity counter simulation

CHAPTER 6. MECHANICAL ASPECTS OF PULL RIG

The RFEC test tool has to be mounted on a mobile platform and be capable of operating at speeds of up to 10 mph. The pull rig has to be able to accelerate the tool up to the desired speed, keep the speed constant during the test and decelerate and stop safely. The pull rig should contain multiple safety measures, because it will be operated in laboratory areas in the presence of people. The tool should create as little noise, vibration or any other disturbance as possible.

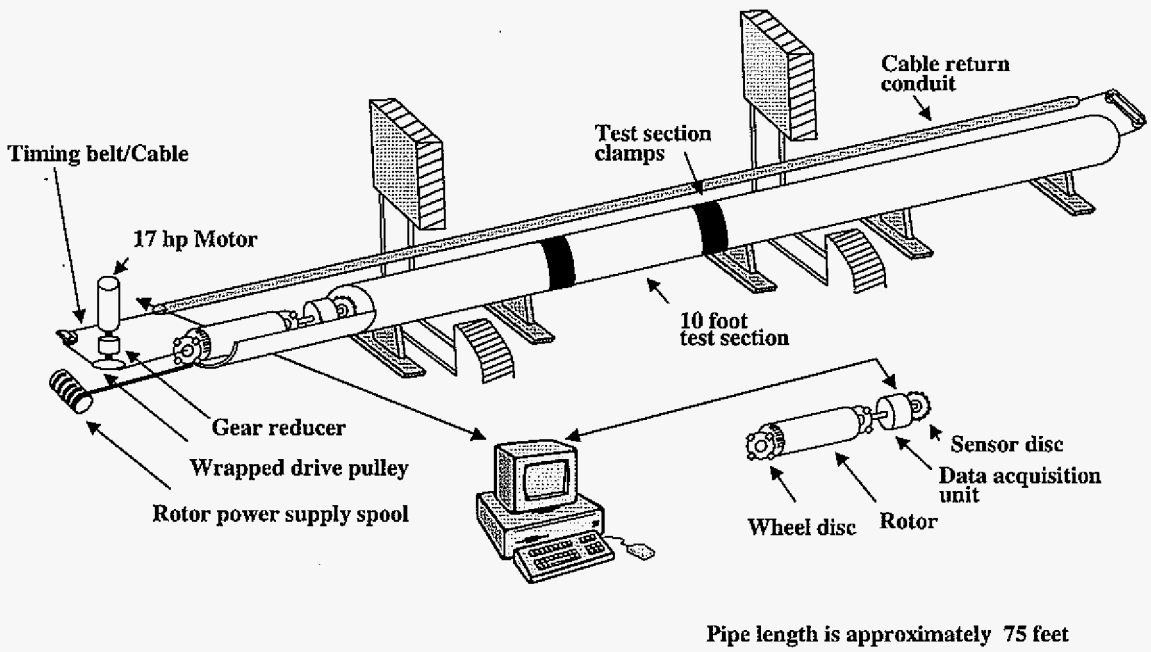

Figure 6.1. RFEC tool and pull-rig

Figure 6.1 shows the major components of the pull-rig. The length of the pipe is approximately 75 feet, spanning three laboratories (as indicated by the partition walls on the diagram). The test section is only 10 feet long. The tool is accelerated by a 17 hp motor and gear-reducer system driving a 140 feet long belt and cable attached to the tool in a closed

loop. The motor is controlled by a micro-controller, which can communicate with a control PC via RS232 interface.

The safety systems implemented on the pull-rig include:

- Mechanical braking system;
- Electrical regenerative braking system;
- Front and back end limit cut-off switches;
- Dead-man switch, requiring operator control during test runs;
- Several feet soft cushion located at the remote end of the pipe;
- Air cushioning;
- Safety measures in the control software (e.g. no open end commands, parameter limit checks);

The safety measures were carefully selected and implemented, such that an adequate amount of safety be provided, without burdening the pull-rig operator. The pull rig is able to move the tool at any point with speeds up to 24 km/h with an accuracy of 2 mm.

CHAPTER 7. CONCLUSIONS

The work presented in this dissertation focused on the development of a non-destructive testing technique based on remote field eddy currents generated by a rotating magnetic field. The conventional MFL testing technology is not capable of detecting axially oriented defects, such as SCC. The main aim of this research was to evaluate if the RFEC-RMF technique can be used to detect not only SCC and in general axially oriented defects, but also other types of defects.

7.1. Summary of accomplishments

Three major contributions of this thesis are: design and developments of the excitation-sensor assembly, static test bed and a fully operational pull rig. As a part of the pull rig, an autonomous inspection vehicle was developed. The inspection vehicle consists of a three-phase rotor, used as an excitation source and a data acquisition system, built on an embedded PC host platform. The data acquisition system consists of an array of sensors and acquisition electronics, coupled to the PC via an FPGA based PCI interface card.

A test bed was developed, which enables non-destructive testing using the RFEC-RMF technique, under static conditions. A feasibility study of the RFEC-RMF method was carried out, in which the magnitude and phase of the voltage induced in a coil positioned under a defect were measured. Four sets of defects were produced in an 8" steel pipe and used in the measurements:

- Axially oriented defects with depths of 20%, 40%, 60% and 80% of the pipe-wall thickness.
- Circumferentially oriented defects with depths of 20%, 40%, 60% and 80% of the pipe-wall thickness.
- Defects skewed approximately 45 degrees to the pipe axis and with depths of 20%, 40%, 60% and 80% of the pipe-wall thickness.

- Round defects with diameter of 1 inch and 1.5 inch and with depths of 20% and 30% of the pipe-wall.

It was found that the RFEC-RMF method is capable of detecting all the defect types. A colony of SCC also produced measurable signal. It was observed that the more the axis of the defect is oriented in circumferential direction, the less information there is in the phase of the measured signal and the more information is contained in the magnitude.

A dynamic measurement system was designed. The mechanical design of the pull rig operation was completely developed, built and tested. Most of the components of the data acquisition system were designed, fabricated, tested and integrated. The FPGA configuration was developed and simulated. The components of the pull rig were developed, tested and installed.

7.2. Future efforts

This work should be continued in the directions outlined below. The efforts should be concentrated on the integration of the data acquisition tool and conducting a parametric study once the tool is operational.

- FPGA configuration: The FPGA configuration has to be finalized in order to continue the development of the embedded PC acquisition software. All the individual elements of the configuration have been developed, but they must be integrated and the integrated circuit must be simulated. It is possible that during the process some changes in the individual elements would be necessary. The next step is floor planning, where the ports of the circuit have to be matched to the pins of the actual FPGA. After floor planning has been done, the configuration has to be programmed in a configuration EPROM.
- Motor control software: The test rig motor control software requires a more effort. A GUI and a set of communication classes were developed. The efforts should be concentrated on implementing and testing safe motion control algorithms. Most of the work can be done without the pull rig being

operational. But, some important components of the control software would require that the pull rig be fully operational, for example, the drive motor would not spin, when it detects that no load is present. In other words, it requires that the inspection vehicle be connected to the pull rig cable, or at least an object of approximately the same weight be used instead.

- Signal processing software. The tool collects the waveforms of the voltage induced in 13 sensors and one reference sinusoidal signal. These signals will be contaminated by noise and will most likely have to be de-trended. The useful information is in the phase difference of each signal waveform with respect to the reference. Once obtained the phase signals will also require processing, such as unwrapping, de-noising, etc. Work on the processing software can commence, once data is collected.
- Parametric studies: The tool is designed to collect signals from SCC but it is important that tool be tested with other defects types, such as saw-cuts, EDM notches. Introducing defects with known parameters into the test section can do this. The effect of tool speed should also be investigated.

APPENDIX A. DAQ BOARDS SCHEMATIC

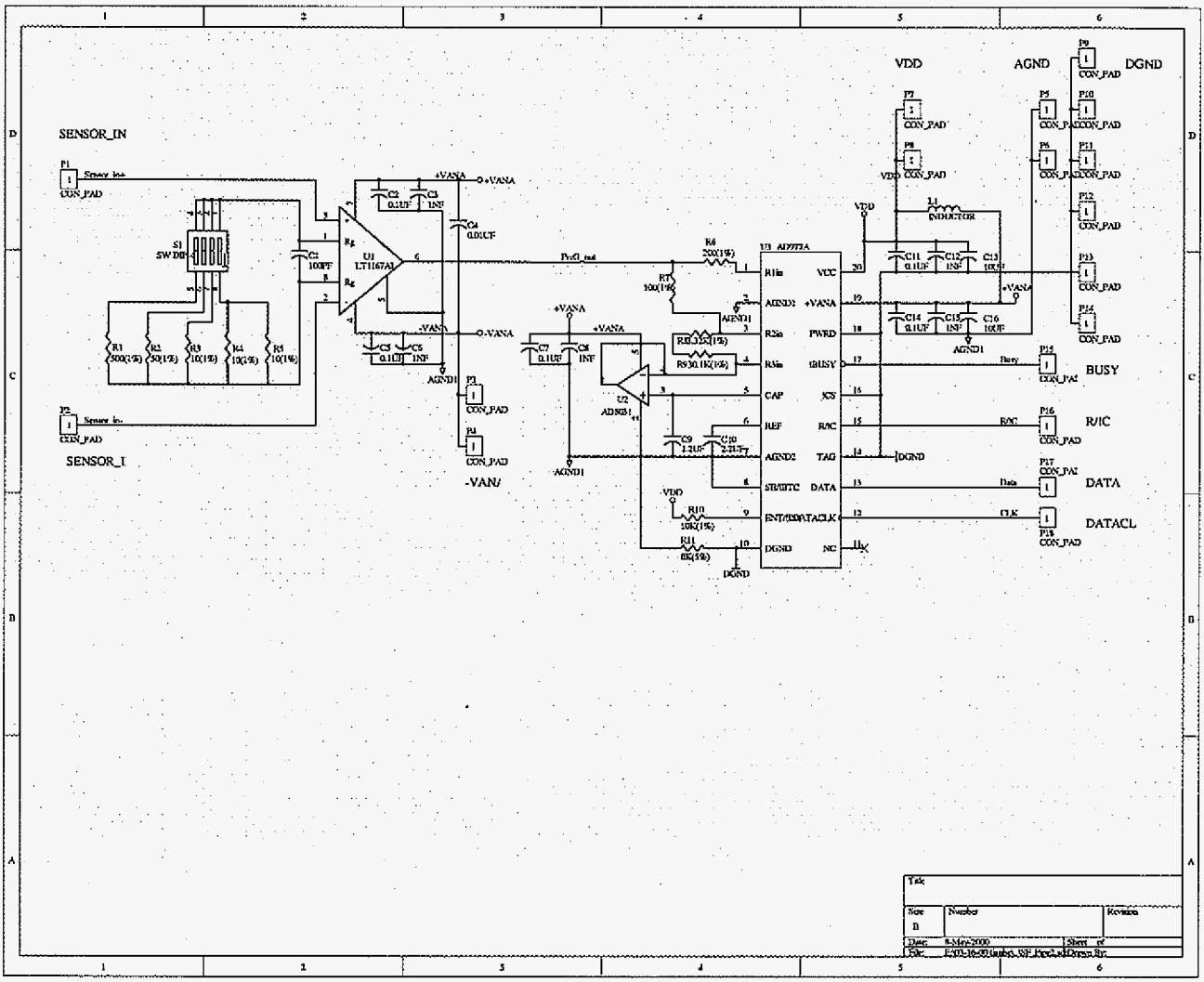

REFERENCES

[1] A. R. Duffy, "The present NG-19 program," 5th Symposium on Line Pipe Research, American Gas Association, Chicago, IL, Paper E, 1974.

[2] L. Udpa, S. Mandayam, S. Udpa, Y. Sun, W. Lord, "Developments in gas pipeline technology," Materials Evaluation, Vol. 54, No. 4, April 1996, pp. 467-472.

[3] T. A. Bubenik, D. R. Stephens, B. N. Leis, R. J. Eiber, "Stress corrosion cracks in pipelines: characteristics and detection considerations," Topical Report GRI 95/0007, Gas Research Institute, Chicago, IL, 1995.

[4] R. L. Wenk, "Field investigation of stress-corrosion cracking," 5th Symposium of Line Pipe Research, American Gas Association, Chicago, IL, Paper E, 1974.

[5] R. N. Parkins, "Factors influencing stress corrosion crack growth kinetics," Corrosion, Vol. 43, No. 3, March 1987, pp. 130-139.

[6] R. N. Parkins, W. K. Blanchard Jr., and B. S. Delanty, "Trans-granular stress corrosion cracking of high-pressure pipelines in contact with solutions of near neutral pH," Corrosion, Vol. 50, No. 5, May 1994, pp. 394-408.

[7] D. D. Mackintosh, D. L. Atherton, P. C. Porter, and A. Teisima, "Test rigs for magnetic flux leakage inspection tools for pipelines," Materials Evaluation, Vol. 50, No. 1, January 1992, pp 13-17.

[8] N. N. Zatsepin and V. E. Scherbinin, "Calculation of the magnetostatic field of

surface deffects. I. Field topography of defect models," Defectoscopia, October 1966, pp. 50-59.

[9] V. E. Scherbinin and N. N. Zatsepin, "Calculation of the magnetostatic field of surface defects. II. Experimental verification of the principal theoretical relationships," Defectoscopia, September-October 1966, pp.59-65.

[10] R. W. E. Shannon and L. Jackson, "Flux leakage testing applied to operational pipelines,""Materials Evaluation, Vol. 46, No. 12, November 1988, pp. 1516-1524.

[11] D. L. Atherton, C. Jagadish, P. Laursen, V. Storm, F. Ham, and B. Scharfenberger, "Pipeline inspection tool speed alters MFL signals," Oil and Gas Journal, Vol. 88, No. 5, January 29, 1990, pp. 84-86.

[12] Y. S. Sun, W. Lord, G. Katragadda and Y. K. Shin, "Motion induced remote field eddy current effect in a magnetostatic non-destructive testing tool: A finite element prediction," IEEE Trans. Mag., Vol. 30, No. 5, September 1994, pp. 3304-3307.

[13] Y. K. Shin, "Numerical modeling of probe velocity effects for electromagnetic NDE," Ph.D. Dissertation, Iowa State University, Ames, IA, 1992

[14] V. K. Zhukov and P. A. Ovsyannikov, "Electromagnetic flaw detector ED-3.02 for inspecting long cylindrical products," Defectoscopia, No. 4, April 1983, pp. 30-35.

[15] V. K. Zhukov, "Feed-through eddy-current transducer with rotating field," USSR Inventor's Certificate No. 580496, Bulleten Izobretenij, No. 42, 1977 (in Russian).

[16] M. Enokizono, S. Nagata, "Non-destructive testing with magnetic sensor using rotational magnetic flux," Journal of the Magnetic Society of Japan, Vol. 15, No. 2, 1991, pp. 455-460.

[17] M. Oka, M. Enokizono, "A detection of backside defect using rotational magnetic flux sensor with search coils," IEEE Transactions on Magnetics, Vol. 32, No. 5, 1996, pp. 4968-4970.

[18] Y. Sun, W. Lord, S. Udpa, L. Udpa, S. Mandayam, "New applications of remote field eddy current techniques," 4th International Conference on the Remote Field Eddy Current Technique, Queen's University at Kingston, Ontario, Canada, August 1997, p. 15.

[19] P. Hammond, J. K. Sykulski, "Engineering Electromagnetism. Physical Processes and Computation," Oxford University Press, 1994, ISBN 0-19-856289-6, pp. 210-213.

[20] W. Lord, Y. S. Sun, S. S. Udpa, S. Nath, "Physics of the remote field eddy current effect," Project PR 179-550, Sept 1986, American Gas Association, pp. 165-172.

[21] W. Lord, Y. S. Sun, S. S. Udpa, S. Nath, "A finite element study of the remote field eddy current phenomenon," IEEE Transactions on Magnetics, Vol. 24, No.1, January 1988, pp. 435-438.

[22] S. Nath, W. Lord, Y. S. Sun, "Theoretical and experimental studies of the remote field eddy current effect," pp. 267-274

[23] T. R. Schmidt, "The remote field eddy current inspection techniques," Material Evaluation, Vol. 42, Feb. 1984, pp. 225-230.

[24] Y. S. Sun, T. Ouyang, S. S. Udpa, "Recent advances in remote field eddy current NDE techniques and their application in detection, characterization and monitoring of deeply hidden corrosion in aircraft structures," Part of the SPIE Conference on Nondestructive Evaluation of Aging Aircraft, Airports and Aerospace Hardware III, Newport Beach, California, March 1999, SPIE Vol. 3586, pp. 200-222.

[25] "16-bit, 100 kSPS/200 kSPS BiCMOS A/D Converter, AD977/AD977A," Analog Devices Technical Manual, Rev. C.

[26] C. A. Holt, "Electronic Circuits. Digital and Analog," John Wiley & Sons 1978, ISBN 0-471-02313-2, pp. 447-448.

[27] "Precision chopper stabilized operational amplifier with internal capacitors," LTC1050, Linear Technology Technical Manual.

[28] "Single resistor gain programmable, precision instrumentation amplifier,' LT1167, Linear Technology Technical Manual.

[29] A. Budak, "Passive and Active Network Analysis and Synthesis," Houghton Mifflin Company, 1974, ISBN 0-395-17203-9, pp. 377-382.

[30] N. Ida, J.P.A. Bastos, "Electromagnetics and Calculation of fields", Springer, 1997, ISBN 0-387-94877-5

ACKNOWLEDGEMENTS

I would like to express my gratitude to my major professor, Dr. Lalita Udpa for providing me with the opportunity to pursue my Ph.D. research at Iowa State University. I very much appreciate the discussions I had with Dr. Satish Udpa and Dr. Yushi Sun.
I would like to thank Dr. David Jiles, Dr. Robert Weber and Dr. Frank Peters for taking their time to serve on my committee.

Thanks must be expressed to Dr. Tianhe Ouyang for her help with the development of the data acquisition system electronics. I would like to tank my colleague Daewon Kim for his contribution to the experimental part of this work. I would also like to thank Dr. Gregory Kobidze for the help he provided with finite element modeling.

This work was performed in part at Ames Laboratory under Contract No. W-7405-Eng-82 with the U.S. Department of Energy The United States government has assigned the DOE Report number IS-T 2354 to this dissertation.